Boundary Layers Affected by Pressure Fields of Adjacent Compressor Blades: A Numerical Approach

by

Jeffrey Santiago Hernández

A Thesis Submitted in Partial Fulfillment of the Requirements for the Degree of
MASTER OF SCIENCE
in
MECHANICAL ENGINEERING
(Thermal-Fluid Sciences)

UNIVERSITY OF PUERTO RICO
MAYAGÜEZ CAMPUS
2018

Approved by:

Sheilla Torres Nieves, Ph.D. — Date
Adviser, Graduate Committee

Jorge Gustavo Gutierrez, Ph.D. — Date
Member, Graduate Committee

Guillermo Araya, Ph.D. — Date
Member, Graduate Committee

Miguel Canals, Ph.D. — Date
Representative of Graduate Studies

Nestor Pérez, Ph.D. — Date
Chairperson of the Department

To my God, wife, Magaly Soto González, and son, Adriel Santiago Soto

Table of Contents

List of Figures

List of Tables

Abstract

Reynolds Average Navier Stoke (RANS) models and Large Eddy Simulation (LES) model, were used to simulate a two NACA 65-410 airfoil compressor cascade using an overset mesh. For mesh validation, comparison of pressure, lift and drag coefficients with experimental data were performed at different angles of attack (*AoA*) for a single NREL S-826 airfoil. Results of the NACA 65-410 compressor cascade at an *AoA* of *0* and *7 deg* with turbulent intensities of *1%* and *6 %* show that LES can capture, with better accuracy than RANS models, the effects produced by the adjacent airfoil in the boundary layer velocities and fluctuations. Also, LES captured flow separation at *74%* of the chord (*c*), confirmed by mean velocity profiles and skin friction coefficient (C_f) calculations. Locations of transition from laminar to turbulent flow were approximated using the C_f. Values were between *41.8%* and *43.7% c*, in agreement with literature.

Resumen

Modelos del Promedio de Reynolds para Navier y Stokes (RANS) y el modelo de vórtices grandes (LES) fueron utilizados para simular dos perfiles alares NACA 65-410 en cascada utilizando una maya quimera. Para validar la maya, coeficientes de presión, sustentamiento y arrastre fueron comparados con data experimental para un solo perfil alar NREL S-826 a varios ángulos de ataque (AoA). Los resultados de NACA 65-410 en cascada, con AoA de 0 deg y 7 deg para intensidades turbulentas de 1% y 6%, muestran que LES posee mejor precisión en modelar los efectos producidos por el perfil alar adyacente en las velocidades y sus fluctuaciones dentro de las capas límites. Además, LES es capaz de capturar separación de flujo a 74% de la cuerda. Localización del punto de transición fue estimada utilizando el coeficiente de fricción, valores entre *41.8%* y *43.7%* de la cuerda fueron obtenidos.

Acknowledgments

First, I want to thank God for the opportunity of pursuing a Master Degree of Science in Mechanical Engineering and be able to fulfill a thesis in the area of computational fluid dynamics. Second, I want to thank my wife, Magaly Soto González, for joining me in this adventure that the world of research can only offers. Magaly, you were always there to give me support when I needed it. With your company and support, I was capable to continue without giving-up. Third, I want to thank my son, Adriel Santiago Soto, to make me understand that the simple details of life are the most important ones. Magaly and Adriel, I love you with all my hart; this job is dedicated to you. Forth, I want to thank my mom, Cándida Hernández Pérez. You teach me that hard work and dedication always pays off, thanks for being an example in my life and to believe in me.

There is a person in particular that I want to acknowledge, my adviser for this thesis Dr. Sheilla Torres Nieves. Thanks for dedicate your time to teach, guide and train me in the amazing world of the boundary layer theory. Most of all, thanks to teach me to think outside of the box, to show me to have passion in what you are doing, and to explore new pathways to make research.

Next, I want to thank Dr. Jorge Gustavo Gutierrez, graduate committee member, for help me to development in the campus of computational fluid dynamics (CFD). Thanks for your time and dedication to give me advises and guide me to the wonderful world of numerical simulation. How to correctly simulate an interrogate a problem to obtain trustworthy data. Also, I want to thank Dr. Guillermo Arraya, graduate committee member, for dedicating his time to provide advice and constructive comments. To help me in the improvement of RANS and LES simulations and to be available for any doubts or question.

For the case of the provision of experimental data for the pressure coefficients of the NACA 65-410 two airfoils compressor cascade and the collaboration in research work, I want to thank Wilmer A. Martinez Valle (graduate student). We had great times doing research together, working with the two airfoils compressor cascade in a numerical an experimental perspective. For sharing knowledge and suggestions, I want to thank the graduate student Carlos J. Quiñones Rodriguez. Also, I want to thank undergraduate students Edwin C. Lopez Ramos and Francesco G. Forina Morales for sharing their knowledge and experience in CFED modeling and in CD-adapco Star CCM+ software. Lastly, I want to thank the support and help of my colleagues in the master degree program; Dick E. Arias González, Angel L. Padilla Viruet, Omar D. Orozco Palencia, Harold H. Valle Reyes and anybody else that collaborated with this work.

CHAPTER 1: INTRODUCTION

1.1 Background

In fluid mechanics, turbulent flows are common in many of today practical problems: internal flow in pipes, two phase flows, atmospheric boundary layers and in turbomachinery components in the airspace industry. Aircraft engines, a type of turbomachinery, are composed of five main components: diffuser, axial compressor, burner, turbine and a nozzle, as shown in Figure 1. These five components are responsible for the propulsion in an airplane. A proper design is needed for each component, specially the axial-flow compressor, since there is a high influence of the development of the boundary layer; hence, understanding the effects of turbulent flow in this component is of great importance.

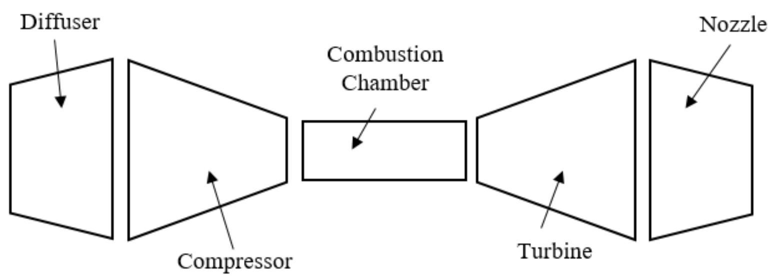

Figure 1: Aircraft engine components

1.1.1 Axial-Flow Compressors

The axial-flow compressor is a dynamic compressor that creates an increment in the fluid pressure by adding energy to the flow; to achieve this, the flow inside the axial-flow compressor goes across many stages that are composed of rotors, and stators (see Figure 2).

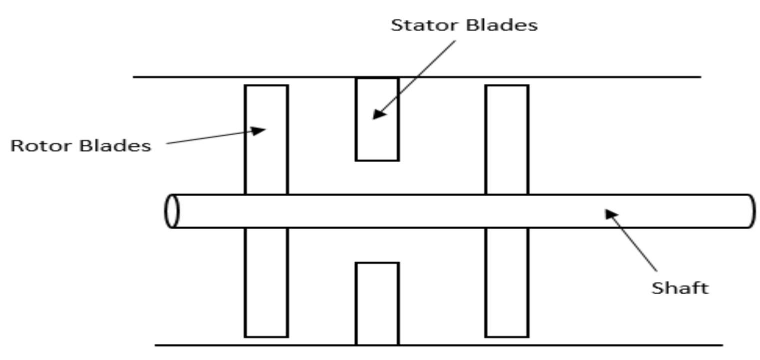

Figure 2: Rotor and Stator Blades in an axial-flow Compressor

Rotor blades are the moving parts that are attached to the shaft and are responsible of adding energy to the fluid increasing the tangential velocity (swirl velocity). Meanwhile, the stator vanes are the steady components that are in charge of converting the kinetic energy to static pressure and to create the proper swirl velocity for the flow that will enter the next rotor stage. These airfoils are aligned with respect to an axis to create a compressor cascade, meaning that the flow that passes between the blades interacts with the upper section of one blade known as suction surface and the lower part of the other, named pressure surface.

For compressor cascade, an airfoil profile that is commonly used is the National Advisory Committee for Aeronautic (NACA) 65, a five-digit family, because of their capacity to distribute the load uniformly. Among the many airfoils that belong to this family, NACA 65-410 is one of the most used and therefore one of the most studied. The first digit means the lift coefficient at the ideal angle of attack, the second digit means the percent of the coordinate parallel to the chord where the camber is maximum, the third digit means if the camber is simple or reflex and the fourth and fifth are the maximum thickness in percent with respect to the chord.

1.1.2 Airfoil Nomenclature

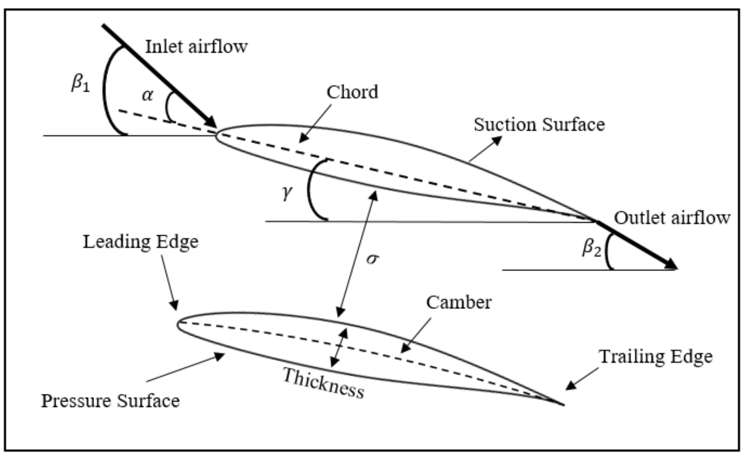

Figure 3: Compressor Cascade Parts

Compressor blades are airfoils that are composed of a leading edge, trailing edge, chamber, chord, angle of attack and percent of thickness. The leading edge is the section of the airfoil where the airflow intersects first, meanwhile the trailing edge is the last section of the airfoil that the airflow leaves. In the case of the chamber line, it is an imaginary line that divides the thickness of the airfoil in haft along the chordwise. When the chord is mentioned, it refers to the imaginary line that connect the leading edge and trailing edge. The angle of attack is an angle formed between the directional vector of the stream flow and the chord line and the percent of thickness is how thick is a section of the airfoil with respect to the chord. In addition, for a compressor cascade design; more parameters are used, these are: flow angle of entrance and exit, stagger angle, turning angle and solidity. The flow angle of entrance is the angle created by the directional vector of the airflow entering the leading edge with the axial direction, in the other hand, the flow angle of exit is the angle between the directional vector of the airflow that exit from the trailing edge and the axial direction. Stagger angle refers to the angle formed by the chord line and the axial direction and the turning angle is the difference of the flow angle of entrance and the flow angle of exit. Finally, the solidity denotes the ratio of the chord line and the critical distance between the adjacent airfoils in a compressor cascade (Aungier, 2003).

1.1.3 Aerodynamic Performance

The two main forces acting on an airfoil are lift force (L) and drag force (D). The majority of the lift force is produced by the difference in pressure, it acts normal to the surface of the airfoil. Also, a small amount of lift can be produced by the component of the shear stress that is normal to the airfoil surface. In the case of the drag force, it is mainly produced by the shear stress parallel to the airfoil surface. Drag force is also produced by the forces due to pressure, that are parallel to airfoil surface. At a zero angle of attack, the drag force produced by the effects of pressure is low, but when the angle of attack starts to increase, the drag force produced by the effects of pressure also increases. To evaluate the aerodynamic performance of an airfoil; lift, drag and pressure coefficients are used. The lift force coefficient is a dimensionless parameter that presents the ratio of the lift force produced by the airfoil surface and the force produced by the dynamic pressure of the free stream. Equation 1 presents the dynamic pressure of the free stream (q).

$$q = \frac{1}{2}\rho U_\infty^2 \tag{1}$$

Where ρ is the density of the fluid and U_∞ is the free stream velocity. Equation 2 describes the lift force coefficient (C_L):

$$C_L = \frac{L}{qS} \tag{2}$$

where S is the area of reference, in the case of the airfoil, the Span (l, length of the airfoil) times the chord (Equation 3).

$$S = l \cdot c \tag{3}$$

For the case of the drag force coefficient (Equation 4), it is the ratio of drag force produced in the airfoil surface and the dynamic pressure force of the free stream (C_D).

$$C_D = \frac{D}{qS} \tag{4}$$

In Equation 5 the pressure coefficient is presented; where the ratio of the dynamic pressure (static pressure (P_{Static}) less total pressure (P_{Total})) produced by the airfoil surface and the dynamic pressure of the free stream is obtained.

$$C_P = \frac{P_{Static} - P_{Total}}{q} \tag{5}$$

For the case of the Skin Friction coefficient (Equation 6), the ratio of the shear stress near the wall and the dynamic pressure of the free stream is obtained.

$$C_f = \frac{\tau_w}{q} = \frac{\mu \frac{du}{dy}}{\frac{1}{2}\rho U_\infty^2} \tag{6}$$

Here, μ is the dynamic viscosity and $\frac{du}{dy}$ is the derivative of the component of the velocity parallel to the wall with respect to the distance normal to the wall. In the case of a flat plate, there are many correlations for C_f, one of these correlations was developed by Smits *et al.* (1983) and is presented in Equation 7.

$$C_f = 0.024 Re_\theta^{-\frac{1}{4}} \tag{7}$$

where Re_θ is defined as the Reynolds momentum thickness (Equation 8).

$$Re_\theta = \frac{\rho L U_\infty}{\mu}, \tag{8}$$

and L is the characteristic length.

1.1.4 Compressibility Effects

Flows are cataloged as compressible or incompressible flow. The Mach number (M), is used to establish if the flow is compressible or incompressible

$$M = \frac{U_\infty}{c} \tag{9}$$

were U_∞ is the stream velocity and c is the local speed of sound. Compressible flow is when the difference in density due to the difference in pressure is significant in the flow. On the other side, incompressible flow is when the difference in density due to the difference in pressure can be neglected.

For incompressible flow, mathematically speaking, velocity and pressure profiles can be solved using the main equations that describe the behavior of the flow; these equations are the continuity and momentum equations. The equation of continuity relates to the concept of mass conservation in a system.

$$\frac{D\rho}{Dt} + \rho\frac{\partial u_i}{\partial x_i} = 0\,, \tag{10}$$

where u_i is the velocity component of the flow, x_i is the coordinate and t represents the time. Since the flow is incompressible, the density is assumed to be constant. Therefore, expanding the equation, the following looks like:

$$\frac{\partial u}{\partial x} + \frac{\partial v}{\partial y} + \frac{\partial w}{\partial z} = 0\,, \tag{11}$$

where u, v and w are the velocity components and x, y and z are the cartesian coordinates. For the momentum equation, a more meticulous analysis needs to be performed. By creating a free body diagram of a package of fluid, normal and shear stress can be obtained. Applying the second law of Newton, the following equation is obtained:

$$\rho\frac{Du_i}{Dt} = \rho g_i + \frac{\partial \tau_{ij}}{\partial x_j}\,. \tag{12}$$

Here, τ is the shear stress. This is known as the Chauchy's equation of motion. Expanding Equation 12, the following expression is obtained:

$$\rho\left[\frac{du}{dt} + u\frac{du}{dx} + v\frac{du}{dy} + w\frac{du}{dz}\right] = \rho g_x + \frac{\partial \tau_{xx}}{\partial x} + \frac{\partial \tau_{xy}}{\partial y} + \frac{\partial \tau_{xz}}{\partial z} \tag{13}$$

$$\rho\left[\frac{dv}{dt} + u\frac{dv}{dx} + v\frac{dv}{dy} + w\frac{dv}{dz}\right] = \rho g_y + \frac{\partial \tau_{yx}}{\partial x} + \frac{\partial \tau_{yy}}{\partial y} + \frac{\partial \tau_{yz}}{\partial z} \tag{14}$$

$$\rho\left[\frac{dw}{dt} + u\frac{dw}{dx} + v\frac{dw}{dy} + w\frac{dw}{dz}\right] = \rho g_z + \frac{\partial \tau_{zx}}{\partial x} + \frac{\partial \tau_{zy}}{\partial y} + \frac{\partial \tau_{zz}}{\partial z} \tag{15}$$

Note that τ_{xx}, τ_{yy}, τ_{zz}, τ_{xy}, τ_{yx}, τ_{yz}, τ_{zx}, τ_{zy} and τ_{xz} are the components of the shear stress tensor. The relationship of the shear stress and the viscosity of the fluid can vary. If the shear stress is proportional to the viscosity then the fluid is a Newtonian fluid, meanwhile if the shear stress is not proportional to the viscosity then the fluid is a non-Newtonian fluid. For a Newtonian fluid, Claude-Louis Navier and George Gabriel Stokes established the constitutive equations and an expression for the shear stress in terms of velocity and pressure is obtained as follows:

$$\tau_{ij} = -P\delta_{ij} + 2\mu\frac{1}{2}\left(\frac{\partial u_i}{\partial x_j} + \frac{\partial u_j}{\partial x_i}\right) \tag{16}$$

Finally, the equations of Navier-Stokes for the momentum in the three cartesian direction are established.

$$\rho\frac{Du_i}{Dt} = -\frac{\partial P}{\partial x_i} + \rho g_i + \mu\frac{\partial^2 u_i}{\partial x_j \partial x_j} \tag{17}$$

1.1.5 Boundary Layers

Fluid problems can be divided into two regions: inviscid region and the boundary layer region. The inviscid region is where the viscous effects are insignificant in the flow. The velocity profile is not affected by the viscous forces, it is only affected by changes in area, geometry, external forces, work or heat transfer. Since the viscous effects are neglected the momentum equations for a Newtonian fluid in the inviscid region are simplified,

$$\rho\frac{Du_i}{Dt} = -\frac{\partial P}{\partial x_i} + \rho g_i\ . \tag{18}$$

These equations are known as the Euler equations, and are only applicable in the inviscid region.

On the other hand, the region of the flow where the viscous effects are significative due to the presence of a surface, that can be a wall, or another fluid, is called the boundary layer region. Velocity profiles situated in this layer are affected in magnitude as the distance from the surface changes. As one gets closer to the surface, the flow has a lower velocity. Because of the viscosity, the layers of the flow, that pass one over another, are affected by a force that opposes movement, or friction, decreasing the velocity of the layer that is on top. This phenomenon will continue until the effects of friction are insignificant and the velocity of the layer will not suffer changes in magnitude. This layer is called the boundary layer. In the case of the flow at the surface $y = 0m$, it will have the velocity of the surface, this is called the no slip condition. Contrary to inviscid flow, the viscous forces cannot be neglected; therefore, no simplification can be made to the momentum equations for Newtonian fluids.

There are two types of boundary layers, laminar and turbulent. In the case of the laminar boundary layer it can be defined as a flow that has streamlines in a parallel direction between them, they do not cross (Post, 2011). Meanwhile the turbulent boundary layer is non-uniform and encounters mixing across its layers.

1.1.6 Turbulent Boundary Layers

Turbulent boundary layer is divided in sublayers that are: outer and inner boundary layer. The inner boundary layer is further divided in the overlap region and viscous sublayer. In turn, this overlap region is segregated in to inertial sublayer and the meso sublayer, while the viscous sublayer is composed of the buffer sublayer and the linear sublayer (George and Castillo, 1997).

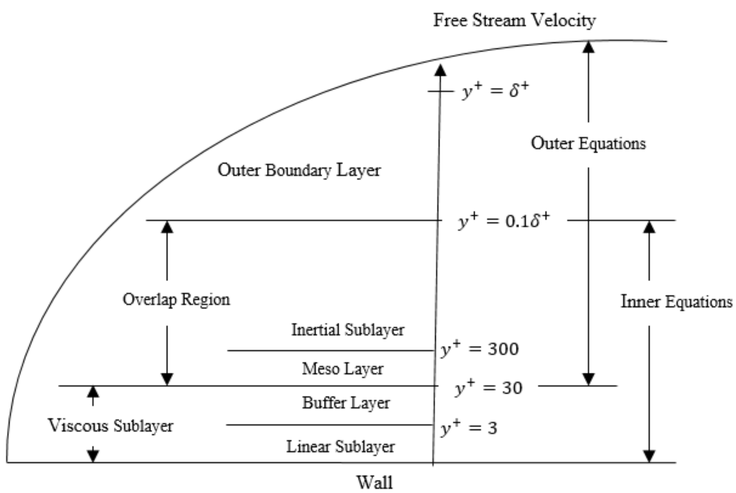

Figure 4: Turbulent Boundary Layer of Smooth Surface (George and Castillo, 1997)

The measurements for the turbulent boundary layer are presented in dimensionless parameters called y^+ and δ^+. The y^+ presents the dimensionless distances normal to the wall and is defined as $y^+ = \frac{u^* y}{\nu}$, were u^* is the shear velocity defined as $u^* = \sqrt{\frac{\tau}{\mu}}$ were τ is the shear stress at the wall and μ is the dynamic viscosity, y is the distance normal to the wall and ν is the cinematic viscosity. For δ^+, it is the dimensionless boundary layer thickness defined as $\delta^+ = \frac{u^* \delta}{\nu}$, were δ is the boundary layer thickness. In the case of the outer boundary layer, the distance from the wall is $0.1\delta^+ \leq y^+ \leq \delta^+$; in this section of the layer the vorticity takes place with no interaction of the viscous forces. For the inertial sublayer, $300 \leq y^+ \leq 0.1\delta^+$, inertial forces dominate over viscous forces and for the meso layer, $30 \leq y^+ \leq 300$, if the Reynolds number is low then viscous forces dominate on this layer but inertial forces effects are also present. In contrast, if the Reynolds number is high, the inertial forces dominate but the viscous forces also have on effect on this layer. For the buffer layer, $3 \leq y^+ \leq 30$, the effect of viscous forces starts to decrease meanwhile the inertial forces start to increase. Lastly, the viscous layer, $0 \leq y^+ \leq 3$, is the layer where the viscous forces dominate; therefore, inertial forces are not present in this layer (George and Castillo, 1997).

1.1.7 Turbulent Boundary Layer Modeling

To solve the velocity and pressure profiles of a turbulent boundary layer, two approaches can be made. One is by solving the instantaneous velocity and pressure profiles, this can be done by solving the Navier-Stokes equations assuming that the dynamic viscosity is constant. The other option is to transform the momentum equations into average momentum equations known as Reynolds Average Navier-Stokes equations. Osborne Reynolds describes that when the amount of time is long enough, the velocity and pressure can be presented as an average value with its fluctuation; that is,

$$\tilde{u} = \bar{u} + u' \tag{19}$$

were $\bar{u}$ is the average velocity and u' is the velocity fluctuation. Substituting the value of the average velocity and fluctuation to the Navier-Stokes equations gives:

$$\rho \frac{D\bar{u}_j}{Dt} = \frac{\partial}{\partial x_i}\left[\mu\left(\frac{\partial \bar{u}_i}{\partial x_j} + \frac{\partial \bar{u}_j}{\partial x_i}\right) - \bar{p}\delta_{ij} - \rho\overline{u_i' u_j'}\right] \tag{20}$$

Equation 6 presents the Reynolds Average Navier-Stokes Equations (RANS). Since the number of variables is more than the number of equations, there is a closure problem; therefore, the RANS equations cannot be solved.

To be able to solve these equations, the number of variables needs to be reduced to the number of equations. These can be done by simulating a turbulent viscosity known as the eddy viscosity, derived from the Buqsiness approximation. This turbulent viscosity theory assumes that the deformation in the vortex (eddy) in the three position coordinates are uniform, meaning that the eddies are isotropic. Eddies are regions of concentrated turbulent kinetic energy that have a structure and energy is transported from more concentration to less. Turbulent kinetic energy is transported from the mean flow to the wall by the eddy cascade were big eddies transport the energy to smaller ones, until the energy is transported to the smallest eddies possible; called the Kolmogorov scale. At this scale, the turbulent kinetic energy by the molecular viscosity is dissipated as heat through the wall. In reality, the small vortices might behave as isotropic but the big ones are typically anisotropic.

The turbulent viscosity model can give good results for problems with simple geometries and low Reynolds Numbers. This model can be resolved by a mixing length scale model or adding additional transport equations to the original RANS equations. The mixing length scale model does not need additional transport equations, it just assumes the turbulent viscosity in terms of a mixing length scale were the turbulent viscosity is defined as:

$$\mu_t = l_m^2 \left| \frac{\partial \overline{U}}{\partial y} \right| \tag{21}$$

l_m is the mixing length scale defined as $l_m = \kappa y$, κ is the Von Karman constant (Pope, 2000).

Mixing length scale can give good results for small eddies where an universal behavior of isotropic behavior can be expected but does not provide good results for large turbulent scales. This model is used in Large Eddy Simulation (LES) (will be discussed later) to simulate the filtered zone since it has a low computational cost and only is used in the small eddy regions. The other approach to solving the turbulent viscosity is by adding additional transport equations, these equations depends on the RANS model that will be used.

There are three principal RANS turbulent models: Spalart Allmaras, Re 2L k-epsilon and k-omega (SST). Spalart Allmaras turbulent model was proposed by Spalart and Allmaras (1994) where they established that by solving only one transport equation, the turbulent viscosity can be determined. It presents excellent results for attached boundary layers, it is used widely for applications in the aerospace industry; however, it is not good for flows with complex recirculation and body forces like buoyancy since it uses the velocity gradient normal to the wall as a reference for the turbulent viscosity calculations. That is, when the separation of the flow occurs the velocity gradient is zero but the turbulent velocity scales are not zero, producing error values in the separation regions. Its main advantage is that it can be solved in a local point, meaning that one point of the mesh does not depend on the other; making the model less expensive computationally, in comparison with the other turbulent models (CD-adapco STAR-CCM+ Version 9.04 User Guide, 2014). The equation for the Spalart Allmaras model, in general form, that solves the modified turbulent viscosity is:

$$\frac{\overline{D}\nu_t}{\overline{D}t} = \nabla \cdot \left(\frac{\nu_t}{\sigma_\nu} \nabla \nu_t \right) + S_\nu \tag{22}$$

Where ν_t is the turbulent viscosity and S_ν is the source terms that are subjected to the laminar and turbulent viscosity (Pope, 2000).

The k-epsilon turbulent model was originated to simulate heat transfer in turbulent fluids (Launder, 1988), and was later modified thanks to the introduction of the Kolmogorov scale (Abe *et al.*, 1993). This model solves a two-equation model, where the transport equations are solved for the turbulent kinetic energy (k) and turbulent dissipation rate (epsilon). It can be used to model complicated flows with separation and heat transfer, an excellent alternative for free convection models (CD-adapco STAR-CCM+ Version 9.04 User Guide, 2014). Turbulent viscosity model only depends on the values of the turbulent kinetic energy and the turbulent dissipation rate, not on the velocity gradient normal to the wall.

$$\frac{\overline{D}k}{\overline{D}t} = \nabla\left(\frac{\mu_t}{\sigma_k}\nabla k\right) + \mathcal{P} - \varepsilon \tag{23}$$

$$\frac{\overline{D}\varepsilon}{\overline{D}t} = \nabla\left(\frac{\mu_t}{\sigma_\varepsilon}\nabla \varepsilon\right) + C_{1\varepsilon}\frac{\mathcal{P}\varepsilon}{k} - C_{2\varepsilon}\frac{\varepsilon^2}{k} \tag{24}$$

Where k is the turbulent kinetic energy, ε is the turbulent dissipation rate, $\mathcal{P}$ the production term, $C_{1\varepsilon}$ and $C_{2\varepsilon}$ are constants for the turbulent dissipation rate equation (Pope, 2000).

The k-omega turbulent model was originated by D. C. Wilcox (Wilcox, 1988). This model, like the k-epsilon one, solves a two-equations model. The transport equation is solved for the turbulent kinetic energy (k) and the specific turbulent dissipation rate (omega); this is defined as the turbulent dissipation rate per unit of turbulent kinetic energy. The k-omega model has an improved performance to simulate the boundary layer under adverse pressure gradient. Its main advantage is that it can be applied to the boundary layer, even viscous-dominated region, without any modification to the code. In the other hand, it has the disadvantage that the modeling of the boundary layer region is sensitive to the value of the specific turbulence dissipation rate in the inviscid region (CD-adapco STAR-CCM+ Version 9.04 User Guide, 2014). The equation for the turbulent kinetic energy is the same as in Equation 16, for the specific turbulent dissipation rate the transport equations is:

$$\frac{\overline{D}\omega}{\overline{D}t} = \nabla\left(\frac{\mu_t}{\sigma_\omega}\nabla \omega\right) + C_{1\omega}\frac{\mathcal{P}\omega}{k} - C_{2\varepsilon}\omega^2 \tag{25}$$

were ω is the specific turbulent dissipation rate, $C_{1\omega}$ and $C_{2\varepsilon}$ are constants (Pope, 2000).

Menter (1994) established a hybrid model that incorporates the k-omega model for the boundary layer region and k-epsilon in the inviscid region to eliminate the sensitivity of the boundary layer model with respect to the specific turbulence dissipation rate.

Another approach to simulating turbulent flows is by the Large Eddie Simulation (LES). It is a hybrid simulation since the regions of the fluid that has most of the turbulent kinetic energy, biggest eddies, are solved numerically and the regions with small eddies, are simulated by the turbulent viscosity model obtaining a filtrated velocity and its residual. The transition from solving numerically to simulating is defined by a filter, basing the transition on the amount of turbulent kinetic energy.

Table 1: RANS Models

<table>
<tr><th>RANS Models</th><th>Advantage</th><th>Disadvantage</th></tr>
<tr><td rowspan="3">Spalart Allmaras</td><td>attached boundary layers</td><td>complex recirculation</td></tr>
<tr><td>flows with mild separation</td><td rowspan="2">body forces</td></tr>
<tr><td>less computational cost</td></tr>
<tr><td rowspan="3">k-epsilon</td><td>complicated flows with separation</td><td rowspan="3">Is not precise near wall simulations as K-Omega</td></tr>
<tr><td>study of heat transfer</td></tr>
<tr><td>free convection models</td></tr>
<tr><td rowspan="2">k-omega</td><td>adverse pressure gradient</td><td rowspan="2">Boundary layer sensitivity</td></tr>
<tr><td>viscous-dominated region</td></tr>
</table>

1.1.8 LES and Integral Length Scales

The energy of the vortex cascade is obtained by an energy spectrum. This spectrum is obtained as follows, if the instantaneous turbulent kinetic energy is obtained in a local region during a certain amount of time, data shown in Figure 5 will be obtained.

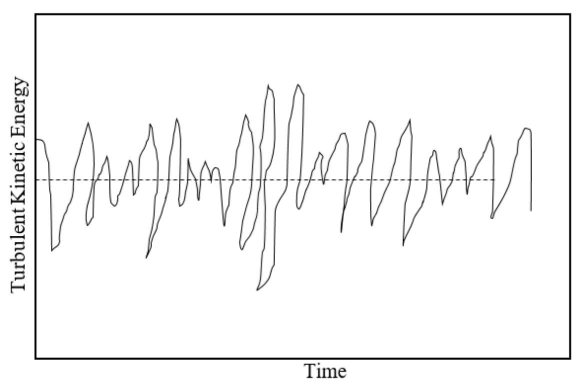

Figure 5: Instantaneous Turbulent Kinetic Energy vs Time

In Figure 5 it can be observed that the velocity varies with time, therefore using the Fast Fourier Transform the time domain can be changed to a frequency domain. Figure 6 shows the magnitudes of the signal that affects the turbulent kinetic energy, the bigger magnitudes are the ones that have a major impact on the fluctuations of the energy. Applying the logarithmic scale in both axis; the Turbulent Energy Spectrum is obtained (Figure 7).

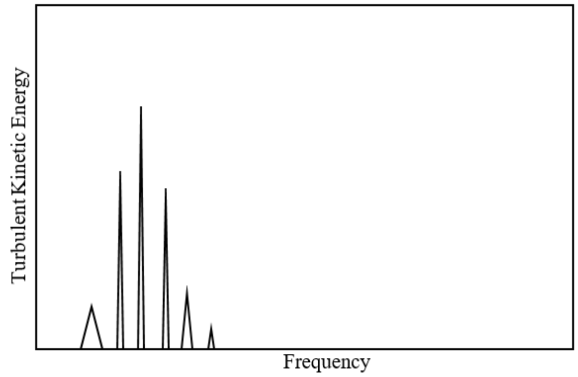

Figure 6: Turbulent Kinetic Energy vs Frequency

This spectrum presents the energy distribution in all the vortex cascade, it can be used to estimate the integral length scale (ℓ_0) since the difference of frequencies are in the same magnitude of the length scale of the eddies. This value represents the average diameter of the eddies enclosed in the spectrum, therefore it represents the scale where most of the energy is located.

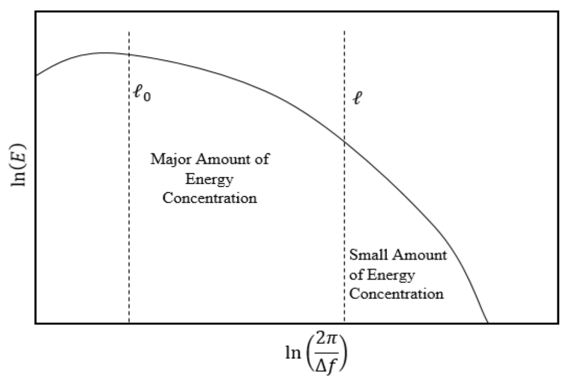

Figure 7: Turbulent Energy Spectrum

In LES, the theory of the filter is based on this spectrum, were the length scale of the filter is smaller than the integral length scale but bigger than the minimum length scale (ℓ) that an eddy can possess, called the Kolmogorov scale. This way, it can solve numerically the major regions of energy concentrations and simulate the rest. The effectiveness, of the LES depends on the mesh resolution, since the grid size need to be in the order of the length scale that capture most of turbulent energy.

There are three types of LES, the Very Large Eddy Simulation (VLES) that the grid size is to course to resolve 80% of the turbulent kinetic energy, Near Wall Modeling Large Eddy

Simulation (LES-NWM) that resolves 80% of the turbulent energy away from the wall but not near the wall and Near Wall Resolution Large Eddy Simulation (LES-NWR), that resolves the 80% of the turbulent kinetic energy far and near the wall (Pope, 2000).

Meany sub-grid filters are used for the LES, but three of the most popular are the classic Smagorinsky filter, Dynamic Smagorisnky filter and Wall Adaptive Local Eddy (WALE) filter. The classic Smagorinsky filter works with a mixing length scale model to simulate the turbulent viscosity and it possess a simple algorithm, the only problem is that it uses a non-changing constant value near the wall region, this provokes instability in the near wall calculations. The Van Driest damping function was created in order to stabilize the model, the only problem is that the function is numerically expensive. It is mainly used to simulate classical problems as references since more advanced filter are elaborate in base of classic Smagorinsky sub-grid algorithm (CD-adapco STAR-CCM+ Version 9.04 User Guide, 2014). The Dynamic Smagorinsky sub-grid filter works in the same way as the classic one, the only difference is that the constant value varies with respect to time, provoking stable solutions in the wall region without the need of damping function. Therefore, the Dynamic Smagorinsky, numerically is less expensive than the classical model and conserve the same properties (CD-adapco STAR-CCM+ Version 9.04 User Guide, 2014). In the case of the WALE sub-grid filter, it is numerically the least expensive filter since it uses the velocity gradients to model the turbulent viscosity in the sub-grid region. It can be used in complex geometry where circulation of the flow occurs and it can produce accurate results near the wall (CD-adapco STAR-CCM+ Version 9.04 User Guide, 2014).

Another way to solve a fluid problem in CFD is by the Direct Numerical Simulation (DNS), where no modeling is used, meaning that all the turbulent scales are solved numerically. Since all the scales of the eddy cascade are solved, the total turbulent energy is solved. In order to create a DNS the mesh needs to be fine enough to solve the smallest turbulent scales that are the Kolmogorov scale, also the time step needs to capture this scales. Therefore, the numerical cost is dramatical and only flow with low Reynolds number can be solved with today's power computation.

Thanks to the computational advances in the past decades, compressor cascades can be simulated numerically. Since the nature of the flow inside the compressor is turbulent, numerical models like Reynolds Average Navier Stoke (RANS), Large Eddie Simulation (LES) and Direct Numerical Simulation (DNS) are used. In the case of LES and DNS, computational cost is a factor that limits the use of these simulations to low Reynolds numbers and simple geometries. In the case of RANS turbulent models, results are an estimation based on assumptions to simplify the turbulent equations; indeed, these turbulent models have a lower numerical cost but the results in the boundary layer region tend to deviate from experimental results. However, because of the low computational cost, RANS turbulent models are the most used in the aerospace industry for computational simulations on turbulent flows.

Since the equations that describe the fluid behavior are complex in nature, RANS models use assumptions to create simple models to present an average solution for the equations, indeed this require minimal resources in computational power and less time to model numerical simulations.

1.2 Motivation

Considering the complexity of the geometry inside a compressor of an aircraft engine and because the fluid behavior is turbulent, it is difficult to perform a numerical solution that can be accurate and, at the same time, have an acceptable numerical cost. Cutting edge technology have allowed for numerical simulations, like LES and DNS, to simulate turbulent flows more precisely. However, because of their computational cost it is only possible to model simple geometries with low Reynolds numbers. Therefore, the aerospace industry relies on other options of simulation, like RANS turbulent models, due to its low computational cost. As much as RANS models can present reasonable results, they still cannot provide accurate data for turbulent flow problems with complex geometries and high Reynolds numbers; particularly in the boundary layer region. This lack of precision can be demonstrated when results of RANS models are compared with experimental results. The main problem is that the limitations of this turbulent models are translated in inaccuracies in predicting the efficiency of turbomachinery since the real effect of the turbulent boundary layers in the compressor are not modeled correctly.

RANS turbulent models are still the tools used in today's aerospace industry. Therefore, the motivation of this work is to present a numerical simulation using RANS turbulent models, to compare with a LES model and experimental data. This will provide better insight into the parameters that must be accurately modeled in order to better predict the behavior of the flows under study. Moreover, this can help to better understand the advantages and disadvantages of each turbulent model and how to combine them in order to have a more precise simulation.

1.3 Objectives

- Perform numerical simulation using an overset mesh and different RANS turbulent models to understand the behavior of turbulent boundary layers.
- Compare RANS models with an LES model.
- Compare numerical simulations with experimental data to validate 2 airfoils compressor cascade computational models and their accuracy.

1.4 Thesis Overview

This thesis is divided in five chapters. In Chapter 2, a full literature review is provided starting to discuss previous work done on computational simulations for compressor cascades. Starting with a brief introduction on the first discoveries done by Archimedes and Leonardo da Vinci., a discussion ensues on how these discoveries impulse a chain of investigations that lead to numerical approaches. Also, it is presented that with help of the increment in computational power thanks to advances in technology, predictions can be done by computational simulations. Lastly, the chapter shows how this opens the door for numerical simulations on airfoils and the application of new methods like, for example, the overset mesh.

Chapter 3 explains the numerical modeling for the computational simulation on a single airfoil NREL S-826 and on a two-airfoil cascade NACA 65-410. Inlet, outlet, and boundary conditions, fluid and modeling properties will be established. Also, details on the mesh and, mesh conditions and parameters are described. Finally, the RANS models selected for the simulation and the LES model are discussed.

As a validation case, preliminary results obtained over a single NREL S-826 using the parameters established in the numerical modeling are shown in section 3.1.1. Results of pressure coefficients and Lift/Drag force coefficients at different angles of attack are discussed with different RANS turbulent models, and compared with experimental data. Plots of pressure coefficients, Lift/Drag force coefficient vs angle of attack and percent of difference were presented and discussed. Also, data validation is presented for the NACA 65-410 two airfoil cascade comparing experimental data of pressure coefficients with LES model.

In Chapter 4, results and discussion for a simulation of a compressor cascade of two airfoils NACA 65-410 is presented. Numerical modeling will be the same as proposed in Chapter 3.

Results for different RANS models will be compared between them, and compared against LES and experimental data. Curves of pressure coefficients for the top and bottom airfoil will be plotted for different turbulence intensities and angle of attack. Also, curves of boundary layers will be plotted for chord positions of *16%* and *74%* and velocities fluctuations for a chord position of *74%*.

Chapter 5 contains conclusions of the accomplishment of the objectives and remarks of results and discussion presented in Chapter 4. At last, Chapter 6 presents modifications of LES mesh and experiments to obtain boundary layers curves, for the NACA 65-410 two airfoil cascade, as future work.

CHAPTER 2: LITERATURE REVIEW

Fluid mechanics is one of the most studied branches in physics. Over decades, numerous persons dedicated their life to understand the basic principles of this science. For example, Archimedes (287-212 B.C.) discovered the fundaments of buoyancy forces by studying objects under a static fluid. Leonardo da Vinci (1452-1519) formulated a mathematical relationship to describe the conservation of mass for incompressible flows in one dimension. Also, one of the discoveries that transformed the studies of fluid mechanics was when Ludwig Prandtl, in 1904, established that viscous forces are present inside a thin layer near the surface of an object, called the fluid boundary layer (Gad-el-Hak, 2016).

Turbulence is a property of the flow and not of the fluid, it is present in most of today's fluid mechanic problems, particularly in the aerospace industry. To understand better the effects of turbulence dimensional analysis are used to obtain dimensionless parameters to characterize the turbulent flow. Some of them are: turbulent viscosity ratio, length scale and turbulent intensity. Mischálek *et al.* (2012) did an experiment with a very high lift low pressure turbine airfoil (T106C) to see the effect of turbulence intensity and Reynolds number values. They used a large scale linear cascade in the VKI S1/C high-speed wind tunnel with a Reynolds number of *80,000* to *160,000* and turbulent intensities from *0.8%* to *3.2%*. The conclusions were that the local Reynolds number depends on the turbulent intensity at separation location and the separation flow transition is dependent on the Reynolds number. Spalart and Rumsey (2017) presents how to correctly used the values of the turbulent viscosity ratio to have good results in computational models. They concluded that very high values of turbulent viscosity ratio can provoke abnormal results in the flow field modeled. To better understand the boundary layer concept, laminar and turbulent flow must be discussed. Laminar flow can be defined as a flow that has streamlines in a parallel direction between them, they do not cross (Post,2011). Meanwhile turbulent flow is described as irregular, has diffusivity and large Reynolds numbers, has fluctuations in three-dimensional vorticity, it is dissipative and continuum (Tennekes and Lumley, 1972).

For the fluid boundary layer, many investigations have been done in order to gain further understanding of the mysteries behind fluid mechanics. The fluid boundary layer is catalogued as laminar or turbulent, also in a laminar boundary layer there can be a transition from laminar to turbulent flow (Schlichting, 1979). Many studies have been done to understand the effects of the boundary layer. Walker and Gostelow (1989) analyses how adverse pressure gradients affect the separation of the boundary layer in a flat plate. They observed that when adverse pressure gradient was high, there was a reduction in transition length. Clemens and Narayanaswamy (2014) made a literature review of how shock waves interacts with turbulent boundary layers, using simple canonic geometries. They established that low-frequency and large-scale unsteadiness are associated with the turbulent boundary layer separation and a model that presents external disturbances that forced interactions which responds like a dynamic system. Schreiber *et al.* (2002) investigated the effects of free stream turbulence and Reynolds number in the boundary layer transition over a compressor cascade. They concluded that for high Reynolds number and turbulent intensity, the transition of the boundary layer was near 7 to 10 percent of the chord. Therefore, high turbulence intensity affects the velocity profile in compressor blades that are designed for high Reynolds number. These studies demonstrate that the behavior of the boundary layer affects the flow over objects like flat plates or airfoils, meaning that the efficiency of turbomachinery is affected.

Turbomachinery is used to create propulsion on aircrafts by compressing, increasing the temperature of air inlet, and expanding the air outlet. The main studied area in turbomachinery is the secondary flow formed because of the rotor and stator components inside. Horlock and Lakshminarayana (1973) measured and studied in an analytical form secondary flow in turbomachinery components. They establish that for the first two or three stages, the flow can be modeled properly, but due boundary layer growing on the walls of the turbomachinery it is difficult to model the rest of the machine. The two principal components that have rotating blades and stator vanes are the turbine and the compressor. However, the compressor is the component most affected by boundary layer development.

The compressor is in charge of creating a pressure ratio greater than one, in order to compress the fluid; in this case air. The blades that are inside, are airfoils that creates the flow movement in the compressor. These airfoils are affected by the turbulent flow produced in the machine. Wherefore, that is why experimental and numerical studies where done over years to get a gasp of why turbulent is produced and how to explained it. Taylor (1978) produced an experiment using probes on a CF6-50 gas turbine engine to studied the compressor outlet stream flow. They concluded that the turbulent intensity of the exit of the compressor was $5\,\%$ of the average steam velocity. The length scale was about $6\ cm$, this number present large vortices.

Camp and Shin (1994) used length scale and turbulent intensity to characterize the turbulent flow on a compressor cascade to obtain inlet values for computational simulations.

In the case of building numerical models to attempt to understand the behavior of fluids in motion, it was until the mathematical derivation of the partial differential equations of fluid motion, better known as Navier-Stokes Equations, that numerical studies will get a relevant position in history. These equations established first by Claude-Louis Navier then revised by George Gabriel Stokes get their place in the hole of fame when Osborne Reynolds incorporates the influence of turbulence in a flow by aggregating additional terms to the Navier-Stokes equation (Post,2011). Using these equations as the fundamental equations to solve a fluid mechanic problem, numerical model where created. In addition, with computational technology; now numerical modeling is a cutting-edge technology that is used by many researchers to study the behavior of flows, specially turbulence. This discipline is called Computational Fluid Dynamics (CFD), one of the pioneers of this branch was Suhas V. Patankar with his classic book *Numerical Heat Transfer and Fluid Flow* (Patankar,1980) where he presented many algorithms to discretize the main differential equations including the Semi-Implicit Method for Pressure-Linked Equation Revised algorithm (SIMPLER algorithm) that correct the pressure values in a incompressible flow model. Wherefore, since this publications toke place; computational models had been developed to be more accurate in their results.

One of the principal studies on compressors are compressor cascades, blades that are collocated in a same rotary axis to move the flow towards the compressor. These studies are specialized on the fluid boundary layer formed in the surface of the compressor airfoils. In computational research, many turbulent models exist; most of them are divided in three main categories: Reynolds Average Navier Stokes models (RANS), Large Eddie Simulations (LES) and Direct Numerical Simulation (DNS). In the case of turbulent RANS models, they are the most used in the industry area to solve turbulent flow problems; because it can present results in a short amount of time due it low computational cost. However, RANS models are not accurate since it approximates the solution of the main equations; therefore, Gourdain *et al.* (2014) established that fluid behavior inside of the compressor is hard to predict and the geometry is too complex. In addition, Schobeiri and Abdelfattah (2013) makes a comparison of RANS and unsteady Reynolds average Navier Stoke (URANS) with experimental results and concluded that for simple problems the numerical results were similar to experimental results; but in complex problems they were not similar. Nevertheless, RANS models are used in many simulations to predict the flow behavior on the surface of different objects. For example: Shiyani and Ankit (2012) have done a computational simulation using Ansys Fluent software on a flat plate using Spalart Allmaras RANS model to obtain the drag and lift force coefficient at different angles of attack. They concluded that these coefficients increase when the angle of attack increases; moreover; they observed that at high angles of attack stall occurs. In the case of numerical analysis of a flow over an airfoil many attempts were done; one of them is Singh *et al.* (2016). An NACA 0012 was studied using k-epsilon turbulent model to study lift and drag force coefficients at different angles of attack. The software used was Ansys Fluent Software and the boundary condition where Velocity Inlet; where velocity, turbulence intensity and turbulent viscosity ratio values were provided and Pressure Outlet, were ambient atmospheric conditions were imposed. They found that when the angle of attack increases, also the lift force coefficient increases, for the NACA 0012 the angle of stall was 16 degree for a velocity of $200\ m/s$. Another investigation similar to the previous one is Dash (2016) that also makes a computational simulation on the NACA 0012 using Ansys Fluent with a k-epsilon turbulent model. The only difference was the comparison between the contours of velocity magnitude and pressure coefficient of the upper part versus the lower part. They concluded that the velocity in the upper region is higher than the lower one and in the case of the pressure coefficient, in the upper part has a negative value and in the bottom one a positive value. Sagmo *et al.* (2016) used a different type of airfoil; NREL S826 for the simulation conducted CD-Adapco STAR CCM+ package. Three RANS turbulent models were used, Spalart Allmaras, k-epsilon and k-omega for two and three-dimension models. The results were compared with experimental data obtained from NTNU and DTU. The assumptions established for the model were ideal gas, compressible and isothermal flow, the Reynolds number for this simulation was *100,000*. The main conclusions were that all RANS turbulent models under predict the value of drag force coefficient in comparison with the experimental results and that for small angles of attack the variations of lift force coefficient between the 2D and 3D simulations are less than for high values of the angle of attack.

Dimensionless values like lift and drag force coefficients are sensible to the solution of the velocity and pressure profile in the fluid boundary layer. Since RANS turbulent models are approximations of the real solutions, dimensionless values are not precise in comparison with experimental data. Therefore, thanks to the technology advances; other models like LES and DNS can be used to solve numerical models for turbulent flows.

In the case of LES turbulent model, it simulates with accuracy the large eddies and ignore the small ones. This model has been used in turbomachinery problems like off-design operating conditions, secondary flows, heat transfer and aero-acoustics (Gourdain *et al.*, 2014). In the other side, this literature review express that LES is used only in simple configurations because of its computational cost. In addition, only a few publications talk about possible recommendations of techniques for meshing procedure of numerical modeling. Medic *et al.* (2016) modeled using LES six different NACA 65 series to compare the numerical results with experimental results of compressor cascades obtained by NACA in the 1950s. In the experiment, the main objective was to predict the transition of laminar to turbulent flow in the boundary layer of the airfoils. The Reynolds number was *250,000* and the computational cost was *20,000 CPU* hours per case. They concluded that the majority of the cases studied in LES, the laminar separation due transition region was predicted.

LES is a powerful tool in numerical simulation of turbulent flows, the only limitation is that it cannot model eddies of small scales. To be able to model eddies of small scales DNS turbulent model is used. In the actuality is the most precise turbulent model since it solves directly the main equations numerically. With DNS eddies in the Kolmogorov scale can be solved. Shan *et al.* (2005) used DNS on a NACA 0012 with an angle of attack of *4 deg* and a Reynolds number of 10^5 to capture the transition, vortex formation, separation and reattachment of the flow. They concluded that the three-dimensional simulation results present a correlation of re-attachment and transition, this can lead to separation control for an airfoil. Balzer and Fasel (2010) made a DNS on a NACA 64_3-618 with angles of attack of *8.64* and *13.85 deg*, and a Reynolds number of *64,200*. This simulation was made to studied the effects of low Reynolds numbers on airfoils of small geometry. For this case, they deduced that the good performance of high angle of attack is because of transition to turbulent near the leading edge bubble on the suction side. Also, Zaki *et al.* (2010) studied the transition of the boundary layer from laminar to turbulent to predict separation in an airfoil. They used a NACA 65 and analyzed the boundary layer in the pressure side and suction side of the airfoil. They observed in the simulation that for the pressure side there was flow separation without the free stream perturbations and no separation when there was free stream forcing. In the case of the suction side, there was separation of fluid independently of free stream conditions.

Even though LES and DNS are the cutting edge technology in academic research, RANS and inviscid models are widely used by the industry since their numerical cost is low and the results obtained are useful even if they are not as precise. This can be seen in simulations on airfoils used in compressor cascades like for example NACA 65-410. For instance, investigations by Madadi *et al.* (2015) and Khazaei *et al.* (2011) conclude that wall boundary conditions for inviscid flow are the most important ones. Both articles established that with additional boundary conditions for the wall, the precision of the solution can be affected, therefore the selection of the additional boundary condition needs to be according with the flow problem.

Different techniques are used to make the simulations more efficient, one of the newest is the overset mesh. It is used in sophisticated simulations like LES; for example Laborderie *et al.* (2016) modeled a high pressure multistage compressor based on a TurboAVBP numerical method that coupled multiple domains with an overset grid method. But, the majority of the applications with overset mesh are used for RANS turbulent models. Floros and Sitaraman (2010) used an overset mesh on a NACA 0015 with a Mach number of *0.1235*, Reynolds number of 1.5×10^6, an angle of attack of *12 deg* and Spalart Allmaras as the RANS turbulent mode. Their main purpose was to validate results with experimental ones. Hoke *et al.* (2009) compared the efficiency of a rigid, overset and deformable mesh to see which gave the best results in a computational analysis of a NACA 0012. The Spalart Allmaras turbulent model was used for this simulation, and concluded that the three methods gave similar results and that it is difficult to recommend one mesh over the other. However, the rigid mesh, that had the lest computational cost, cannot be used in moving objects simulations like the overset or deformable mesh.

CHAPTER 3: NUMERICAL MODELING

3.1 Validation Case

For the numerical simulation, a commercial computational fluid dynamic (CFD) software, CD-adapco STAR-CCM+ 11.04.010 was used. The specimen for the analysis was an airfoil NREL S-826 with a chord of $0.45\ m$. The fluid used for this model is air with a density of $\rho = 1.18\ kg/m^3$ and a dynamic viscosity of $\mu = 1.855 * 10^{-5}\ {m * s}/{kg}$. The flow was assumed to be incompressible with a Reynolds number of $Re = 100{,}000$. Meanwhile, the velocity inlet was $3.48\ {m}/{s}$ with a pressure reference of $P = 101.325\ kPa$. Turbulent parameters were a turbulent intensity of 0.71% and a turbulent length scale of $0.1355m$. These conditions were selected to replicate those from Sagmo et al. (2016) in an effort to validate our results.

The mesh used for this simulation was a polyhedral mesh for the volume mesh, a surface remesher for the surface mesh and a prism layer mesher to model the boundary layer at the wall of the airfoil. Since the scaling for the percent of the base size is designed for an airfoil with a chord of $1\ m$, all the parameters of the background mesh, overset mesh and control volumes are based on a chord of $1m$. Then, an option of scale mesh is applied with a factor of 0.45, to shrink the airfoil chord to $0.45\ m$ and all the other parameters will adjust to this chord. The domain of the fluid was discretized in a background mesh with dimensions of $22.5\ m$ in length, $10\ m$ in height, and a base size of $0.5\ m$. The background mesh was initialized with an overset mesh to allow for performing the analysis of the airfoil under different angles of attack using the same mesh modeling. The mesh parameters of surface growth rate were 1.15 for the overset mesh and 1.05 for the background mesh.

The overset mesh had dimensions of $4\ m$ in length, $2\ m$ in height and a base size of $0.5\ m$. Four volumetric controls were developed in order to have a better precision when data is recollected. These are the overlap, airfoil overlap, airfoil, downstream and small volume controls for the leading and trailing edge. In the case of the overlap, it is used in both meshes as a smooth transition from the background mesh to the overset mesh; this allows a better communication between both meshes. The overlap volumetric control had a dimension of $6\ m$ in length and $4\ m$ in height, and the percent of the base size was $12.5\ \%$. In the other hand, the rest of the volumetric controls are applied only to the overset mesh.

Figure 8 identifies, the background mesh (1), overset mesh (2), overlap (3), downstream (4), airfoil (5) and airfoil overlap (6). The leading and trailing edge volumetric regions are small and cannot be seen in detail in Figure 8; these are located inside the prisms layer region as cylindrical shape (radius of $0.007\ m$ and a percent of base side of 0.1%) for the leading edge and a rectangular shape ($0.01\ m$ in length, $0.001\ m$ in height and a percent of base side of 0.034%) for the trailing edge to refine the complex curves in both ends of the airfoil. Table 1 shows the dimensions and percent of base size.

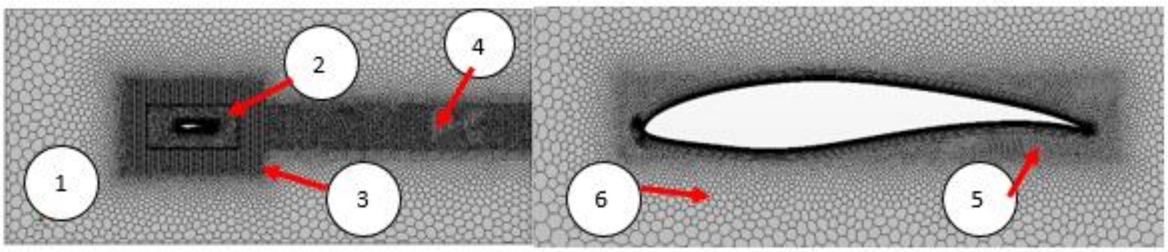

Figure 8: Meshes and Volumetric Controls

Table 2: Volumetric Control Parameters

Volumetric Control	Dimensions		Percent of Base Size
	Length (m)	Height (m)	
Airfoil Overlap	1.66	0.41	5.0%
Airfoil	1.12	0.17	1.0%
Downstream	16.08	1.93	12.5%

Boundary conditions are applied to the background mesh. In order to simulate an incompressible fluid, the inlet of the fluid is modeled as a velocity inlet boundary condition, outlet of the fluid as pressure outlet boundary condition and top and bottom of the domain as a symmetry boundary condition. In the case of the overset mesh, the surface of the airfoil is designated as solid with a no slip condition. Wall treatment was developed on the surface of the airfoil, consisting of a prism layer with 30 layers and $y^+ = 0.45$.

The wall treatment for the model was low y^+ treatment for Spalart Allmaras and k-omega (SST) models and all y^+ treatment for Realizable two layers k-epsilon. Subsequently, the model parameters were as follow: the simulation was analyzed in two dimensions, steady state, ideal gas, segregated flow and constant density. Three Reynolds Average Navier Stokes (RANS) turbulent models were used for this simulation: k-epsilon, k-omega and Spalart Allmaras.

3.1.1 Data Validation

As a validation case, simulations of only one airfoil NREL S-826 were done and results were compared with experimental data for the same NREL model with a Reynolds number of 100,000, turbulence intensity of 0.71% and a turbulent length scale of $0.1355\ m$. In the case of empirical data, Norwegian University of Science and Technology (NTNU) pressure tap experimental data (Aksnes, 2015) and Technical University of Denmark (DTU) up stroke experimental data (Sarlak et *al.*, 2014) are selected to validate the simulations. In a wind tunnel Aksnes used pressure taps on a NREL S826 airfoil with a chord of $0.45\ m$ and a spam of $1.8\ m$ to calculate the lift, drag and pressure coefficients; most of the values where reported without the correction of the 8% of blockage. The percent of turbulence was 0.71% and the turbulent intensity was $0.1355m$. In the other hand Sarlak et *al.* (2014) used the same airfoil with a chord of $0.1\ m$ and a spam of $0.5m$, they measured the lift coefficient by force gauge and the drag coefficient by integrating the wake profiles in the downstream. Pressure coefficient was measured with pressure taps, the measurements where obtained in a low speed wind tunnel. The turbulent intensity was 0.2%. Data obtained by RANS simulations of Sagmo et al. (2016) are used for the validation as well. Dimensionless parameters like lift force and drag force coefficients were obtained at different angles of attack and then compared with NTNU and DTU experimental data. Furthermore, three turbulent models where used for the simulations; Spalart Allmaras, Re 2L k-epsilon and k-omega (SST) turbulent models. For each simulation, the iterations were between $1{,}900$ and $9{,}000$ iterations, with residuals between $4 * 10^{-4}$ and 10^{-13}.

On the following plots, the symbols represent the experimental data sets; the other curves represent the turbulent models. Figure 9 depicts the relation between lift force coefficient and angle of attack. As expected, the lift force coefficient increases as the angle of attack increases. As has been noted, the three turbulent models provided similar results in comparison with NTNU, DTU and Sagmo et *al.* (2016) data. When compared to other numerical simulation, the values show good agreement; on the other hand, it can be observed that the three RANS simulations are closer to the values of DTU rather than NTNU values.

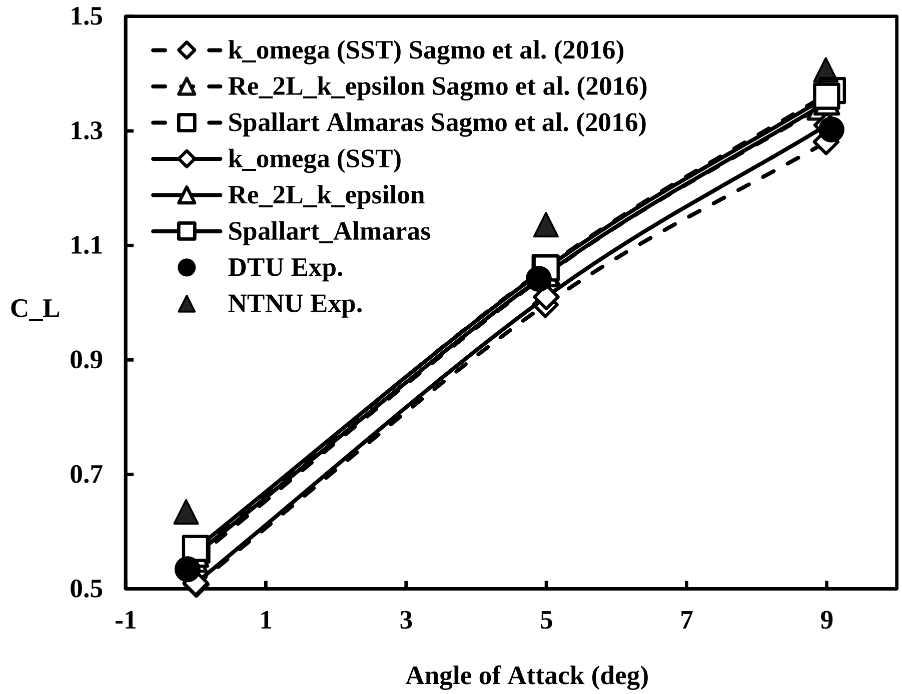

Figure 9: C_L vs Angle of Attack

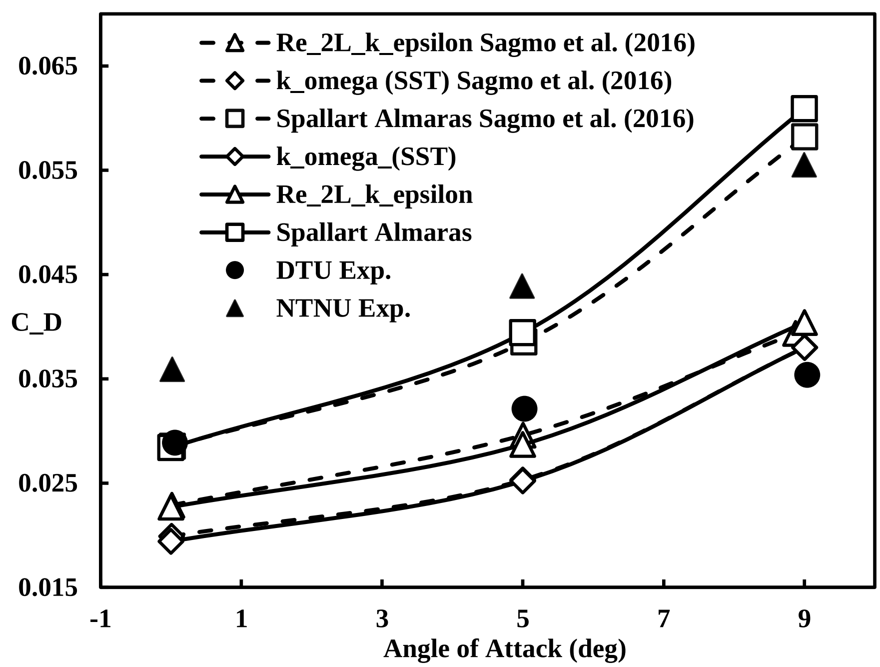

Figure 10: C_D vs Angle of Attack

In Figure 10, curves of drag force coefficient vs angle of attack are presented. In contrast to Figure 9, where plots have a more linear behavior, Figure 10 shows a parabolic one, independent of the angle of attack magnitude. This behavior is because the drag force is caused by shear stresses parallel to the airfoil surface, producing a force in the direction against movement regardless of the angle of attack magnitude.

In the case of Figure 10, the turbulent models show more disagreement with respect to the experimental data, but among simulations, the results of C_D are similar, but between each RANS model the values have discrepancies. Spalart Allmaras has the higher values of C_D in magnitude, followed by Re 2L k-epsilon and k-omega (SST) that are more conservative. For each angle of attack there is one model that predicts the C_D closer to the experimental values than the rest, for instance using the DTU data as reference, Spalart Allmaras has a closer value of C_D to the experimental data at 0 deg, Re 2L k-epsilon at 5 deg and k-omega (SST) at 9 deg.

As shown below in Table 2, the percent of difference for C_L for most of the cases have acceptable values. Lower magnitudes can be seen with respect to DTU experiment values rather than NTNU ones. It is important to highlight some of the main differences between the two experimental data sets used. To understand these differences, the experiments were taken in different facilities, the angle of attack between NTNU and DTU was shifted by *1.5 deg*, the amount of time for each measurement of C_L and C_D was *60 seconds* in the case of NTNU and only *10 seconds* in the case of DTU, the aspect ratio of the wind tunnel at NTNU was *4* and for the case of DTU was *5*, and NTNU data was obtained by pressure taps and DTU by upstroke.

Table 3: Percent of Difference of C_L for Turbulent Models

AoA (deg)	Experiments	% Diff. C_L					
		k omega (SST) Sagmo et. al (2016)	Re 2L k epsilon Sagmo et. al (2016)	Spalart Allmaras Sagmo et. al (2016)	k omega (SST)	Re 2L k epsilon	Spalart Allmaras
0	DTU Exp.	5.0	3.3	6.2	4.5	4.8	6.6
	NTNU Exp.	22.2	14.0	11.1	21.7	12.4	10.7
5	DTU Exp.	4.4	0.9	1.8	3.1	0.8	1.8
	NTNU Exp.	13.1	7.8	6.9	11.7	7.9	6.9
9	DTU Exp.	1.7	3.0	5.1	0.6	3.6	4.4
	NTNU Exp.	9.4	4.7	2.6	7.1	4.1	3.4

Table 3, shows the percent of difference for C_D compared to NTNU and DTU experimental data. In contrast with values of Table 1, the percent of difference are higher in magnitude; however, the comparisons of simulation vs simulation are similar. For each angle of attack there is a RANS model that has a percent of difference much lower than the other ones. For this case, the difference between the NTNU and DTU experimental data are less than the C_L case.

Table 4: Percent of Difference of C_D for Turbulent Models

AoA (deg)	Experiments	% Diff. C_D					
		k omega (SST) Sagmo et. al (2016)	Re 2L k epsilon Sagmo et. al (2016)	Spalart Allmaras Sagmo et. al (2016)	k omega (SST)	Re 2L k epsilon	Spalart Allmaras
0	DTU Exp.	36.7	23.1	1.2	39.2	23.9	1.6
	NTNU Exp.	57.3	44.3	23.0	59.7	45.1	23.3
5	DTU Exp.	23.7	8.2	18.1	24.1	11.2	20.4
	NTNU Exp.	53.7	38.9	13.0	54.1	41.8	10.8
9	DTU Exp.	7.2	10.6	48.8	7.2	13.3	53.0
	NTNU Exp.	37.4	34.1	4.7	37.5	31.5	9.2

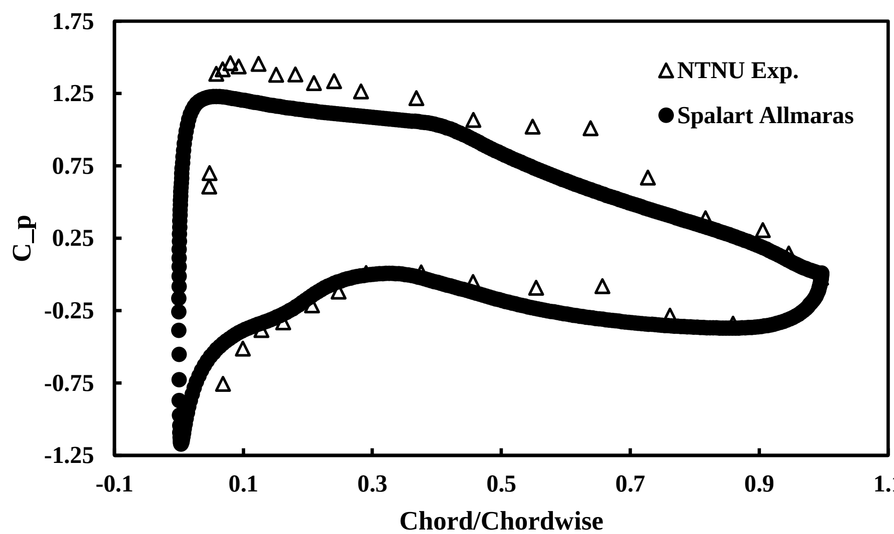

Figure 11: C_p vs Chord/Chordwise

Figure 11 presents a plot of the pressure coefficient (C_p) vs Chord/Chordwise. The values of the experimental data versus the model 2D Spalart Allmaras are similar in behavior and in magnitude. In contrast with the data of C_L and C_D, the NTNU values approximates better with the RANS model since the data was provided by pressure taps, making the measurements more accurate. For this case only, the model of Spalart Allmaras was used to validate the mesh with the results of Sagmo et *al.* (2016), since they established that 2D Spalart Allmaras has good results in comparison with the experimental data.

3.2 RANS and LES Numerical Setup

For the two airfoil cascade simulations, the airfoil NACA 65-410 was used with a free stream velocity of $u_\infty = 10\ m/s$, a density of $\rho = 1.18\ kg/m^3$ and a dynamic viscosity of $\mu = 1.86x10^{-5}\ \frac{m \cdot s}{kg}$. The chord value was $c = 0.09m$ with a solidity of $\sigma = 1.5$, the Reynolds number with respect to the chord was $Re = 57{,}097$. Note that the range of the critical Reynolds number of a NACA 65-410 airfoil can be approximated between the critical Reynolds number of a cylinder ($Re_{cr} = 200{,}000$), since the leading edge has a blunt shape similar to the cylinder, and the critical Reynolds number of a flat plate ($Re_{cr} = 500{,}000$); the rest of the airfoil body is similar in geometry to a flat plate.

The physical models were two-dimensional (RANS models) and three-dimensional (LES model), steady state (RANS models) and implicit unsteady (LES model), incompressible and segregated flow. Study cases are presented in Table 4.

Table 5: Study Cases

AoA (deg)	Turbulent Intensity (%)	Velocity (m/s)	Turbulent Model
0	1	10	Spalart Allmaras
			Two Layer Realizable k-epsilon
			k-omega (SST)
			LES
	6		Spalart Allmaras
			Two Layer Realizable k-epsilon
			k-omega (SST)
			LES
7	1	10	Spalart Allmaras
			Two Layer Realizable k-epsilon
			k-omega (SST)
			LES
	6		Spalart Allmaras
			Two Layer Realizable k-epsilon
			k-omega (SST)
			LES

For the simulations the boundary conditions were velocity inlet, pressure outlet, wall in the surface of the airfoil and symmetry condition in the stream-wise boundary. The turbulent models selected were the RANS models Spalart Allmaras, Realizable two Layers k-epsilon, k-omega Shear Stress

Tensor and the Large Eddie Simulation. Turbulent intensities of $TI = 1\%$ and $TI = 6\%$ were used in combination with angles of attack of $AoA = 0\ deg$ and $AoA = 7deg$. An $AoA = 7deg$ was chosen since it was the highest AoA at which the three RANS models converge while still being close to the stall angle.

For the LES model, a three-dimensional domain was used with an overset mesh, where the streamwise and normal directions were meshed with a polyhedral mesh and the span direction employed a structured mesh. The wall distance was selected in order to accomplish a normal distance (y^+) $y^+ < 1$ for the $AoA = 7deg$ since it has the highest shear velocities u_τ because of the curvature effects. Taking this into consideration, $y^+ = 0.9$ was selected for the highest local u_τ in the $AoA = 7deg$, therefore each local $y^+ < 1$ for $AoA = 0deg$ and $AoA = 7deg$. The chord distance (x^+) was selected to be $x^+ = 130 \cdot y^+$ and the spam distance was selected to be $z^+ = 40 \cdot y^+$.

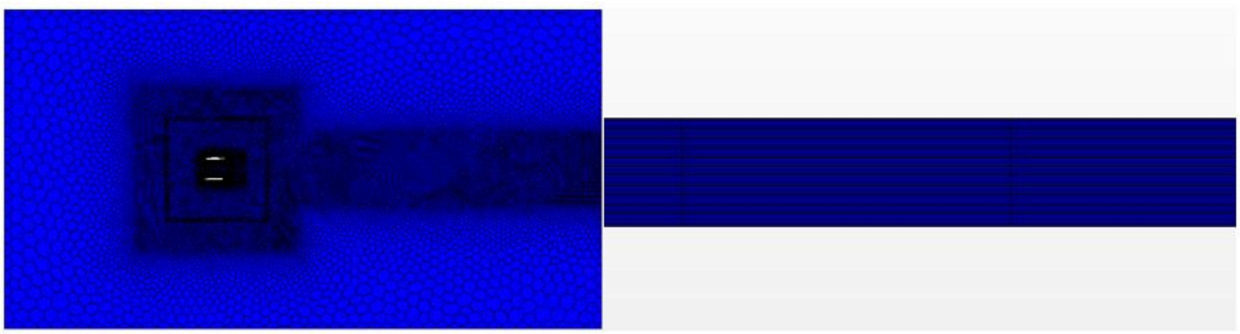

Figure 12: Hybrid Mesh for LES (a) Polyhedral Mesh, (b) Structure Mesh

The mesh parameters and volumetric controls were the same as in the validation case with the exception that, since there are two airfoils and the volumetric controls are applied for each airfoil, the Airfoil volumetric control percent of base side is 1.26% and the prism layer of both airfoils have 65 layers. Since the chord is $0.09m$, now the factor of mesh scale changes to 0.09, meaning that the parameters of the mesh will be affected by this value. For the case of the RANS model, the same mesh of the LES simulation is used; this will ensure mesh-independence in the RANS model vs LES model comparison. The mesh was transformed into two-dimensional, converting the hybrid mesh into a polyhedral mesh.

For the LES model, a Dynamic Smagorinsky sub-grid model was selected. The time step was selected to be $t = 4.075x10^{-5}s$ for $AoA = 0deg$ and $t = 1.504x10^{-5}s$ for $AoA = 7deg$. These time steps are ten times the Kolmogorov time scale $10 \cdot t^+ = (10 \cdot t) / \left(\frac{\nu}{(u_\tau)^2}\right)$. First the three-dimensional problem was simulated with a k-omega (SST) model to have an approximate value for the velocity and pressure contours, then these values were used as an initial condition for the LES simulation. The time that the flow took to pass from the leading to the trailing edge was calculated as $T = \frac{c}{U_\infty}$, this value is used as the reference time for the statistic calculations. To ensure that the flow converged statistically, the LES simulation was ran for a time period of two times the reference time ($2 \cdot T$), then samplings were taken for each time step for a time equivalent to five times the reference time ($5 \cdot T$). The total time for the simulation run was seven times the reference time ($7 \cdot T$). Finally, the statistical data obtained were the velocity average and fluctuation, pressure average and the average coefficient of Lift and Drag force.

3.2.1 Measurements

The final data that was collected is the velocity and its fluctuations to plot curves of the boundary layer and fluctuations in the three directions. The data was obtained from the suction side of airfoil 1 (top airfoil) and airfoil 2 (bottom airfoil). Two locations were studied in detail: pressure tap 1, at 16% chord, and pressure tap 5, at 74% chord. Figure 13, shows the airfoils and the pressure tap locations.

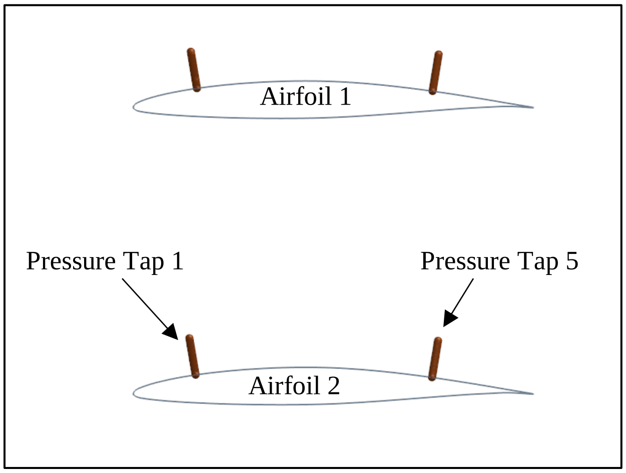

Figure 13: Diagram of Airfoil 1 and 2 with Pressure Taps 1 and 2

3.2.2 Data Validation

In Figure 14, pressure coefficient vs percent chord is plotted for airfoil 2. LES data for turbulence intensity of *1%*, at an angle of attack of *0 deg*, is compared with experimental data provided by the research work of graduate student *Wilmer A. Martinez Valle*. In the case of the experimental data, it was taken in a wind tunnel with a turbulence intensity between *0.1%* and *1%*. The time step for the experiment was *1ms* and *5,000* samples were gathered. The angle of attack for the airfoil was *0 deg*. Comparing LES model and experimental data, it can be observed that the behavior of the experimental data is showing a similar behavior than that predicted by the simulation. In terms of precision, there are some regions that differ significantly. This phenomenon can be produced by deformations in the airfoil surface and/or manufacturing imperfections, slight differences in turbulence intensities and statistical errors, since the LES model has a lower time step and a higher sampling rate.

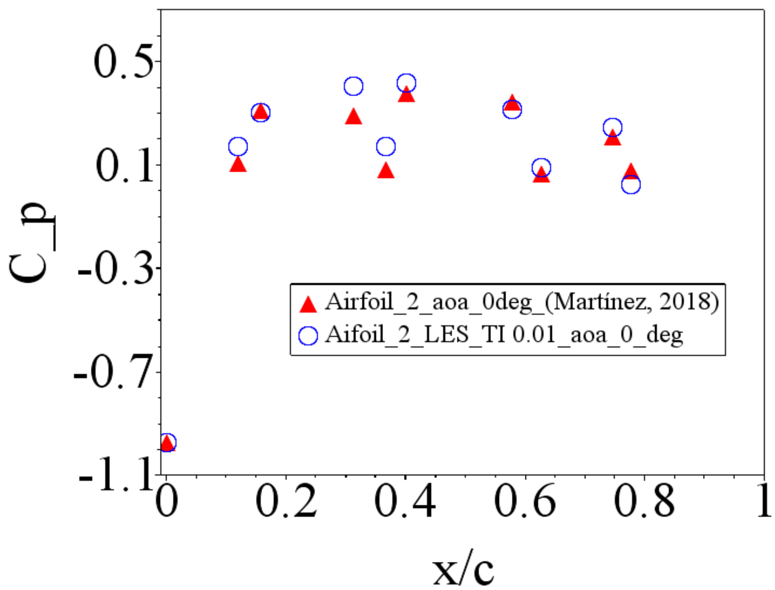

Figure14: Cp vs x/ch for LES vs Experimental Data, Airfoil 2

Chapter 4: Results and Discussion

4.1 Pressure Coefficients for Airfoil 1 and 2

In Figure 15 curves of pressure coefficient vs percent chord, for the airfoil cascade at different angles of attack and turbulent intensities, are compared for different RANS models.

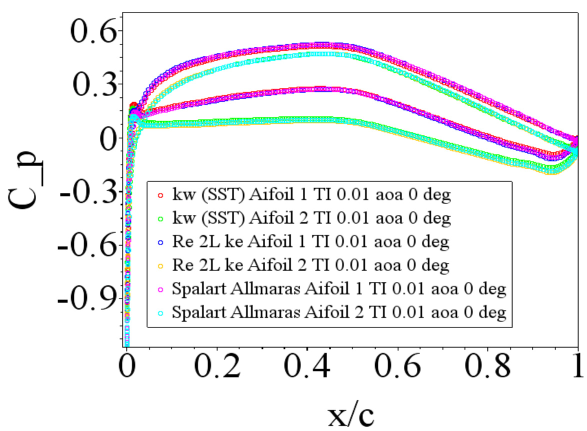

(a)

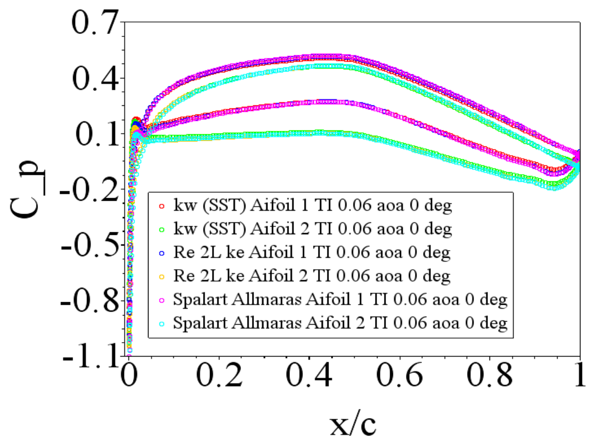

(b)

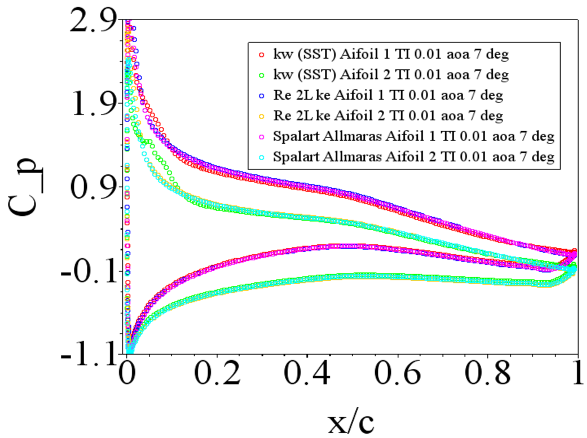

(c)

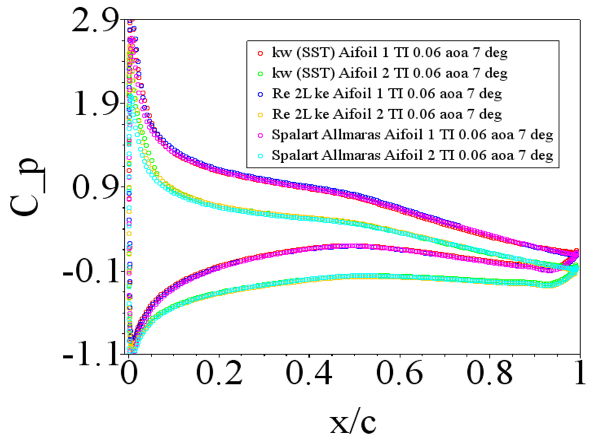

(d)

Figure 15: Cp vs x/ch RANS models, (a) AoA of 0 deg with TI of 1%, (b) AoA of 0 deg with TI of 6%, (c) AoA of 7 deg with TI of 1% and (d) AoA of 7 deg with TI of 6%

The behaviors of the plots are as expected, based on the theory. For *AoA* of *0 deg* (Figure 15a and 15b) the difference in area under the curve, between the suction and pressure sides, is not so pronounced; the difference in pressure is small. Meanwhile, for *AoA* of *7 deg* the difference in area under the curve increases with respect to turbulence intensities of 1% and 6%; the differences in pressure are significant since the flow in the suction side is accelerating more than the flow in the pressure side. It is notable that for the suction and pressure side, for *AoA* of *0 deg* and *7 deg* (Figure 15a, 15b, 15c and 15d), near the leading edge, the curve of the pressure coefficient sees a significant increase. Then, at about 50% chord, the pressure coefficient starts to decrease. This phenomenon occurs because of the pressure gradients. Near the leading edge, the thickness of the airfoil is increasing; this is designed so the flow experiences favorable pressure gradient and, hence, the flow is accelerating. Then the thickness reaches its maximum value and starts to decrease, producing an adverse pressure gradient, meaning that the flow decelerates when it is moving toward the trailing edge. The final design is to produce the optimum aerodynamic performance while, at the same time, to prevent flow separation. Therefore, the presence of favorable and adverse pressure gradients creates an increase in the velocity near the leading edge and the pressure coefficient increases, and a decrease in velocity near the trailing edge results in lower values of pressure coefficient.

Viewing the four figures (Figure 15a, 15b, 15c and 15d), it can be observed that the curves of the three RANS models collapse with each other, meaning that the turbulent models provide similar results for the dynamic pressure near the wall of the airfoils. Comparing airfoil 1 with airfoil 2 (see position of airfoil 1 and 2 in Figure 15), it can be observed that the curves are similar but they are shifted in the dependent axis. When the *AoA* is at *0 deg*, the difference in the suction side is not so evident than in *AoA* at *7 deg*. The curve of airfoil 1 has higher pressure coefficient values in the suction side (top part of the curve) since there is more acceleration of the flow, due to the free stream condition were no additional object is disturbing the flow. On the other side, airfoil 2 feels the presence of airfoil 1 in the suction side; it encounters a throat that accelerates the free stream flow that passes between them. This affects the performance of airfoil 2 because the curvature of the body cannot produce an adequate acceleration due to the throat effect, resulting in a higher dynamic pressure in the suction side this means that the velocity is lower than in the suction side of airfoil 1. For the case of the pressure side, airfoil 1 is affected with the presence of airfoil 2. Since the throat is accelerating the flow between the airfoils, the pressure side of airfoil 1 has higher velocities than the pressure side of airfoil 2. Therefore, this provokes lower of pressure levels in the pressure side affecting the normal forces distribution over the airfoil surface.

For the case of the difference in turbulence intensity, for *AoA* of *0 deg* and *7 deg* (Figure 15a, 15b, 15c and 15d); the curves in Figure 15a vs Figure 15b and Figure 15c vs Figure 15d, are similar in magnitude. Therefore, the results of the pressure coefficients for RANS models are not sensible to changes in the turbulence intensity of the free stream region.

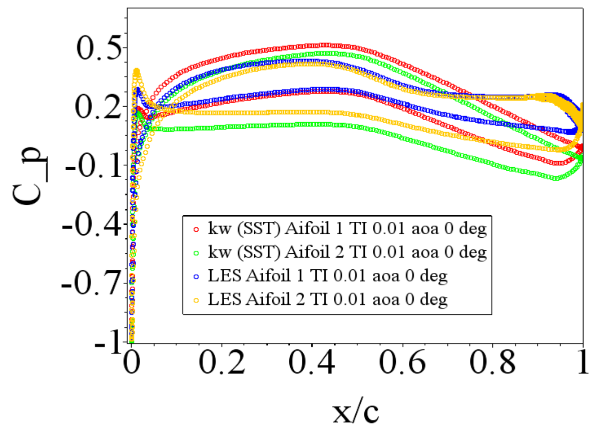

(a)

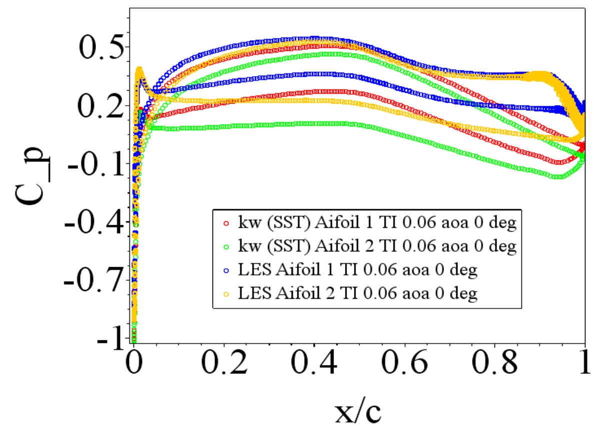

(b)

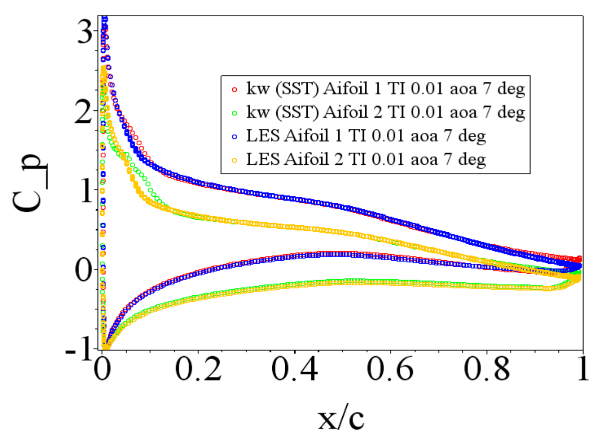

(c)

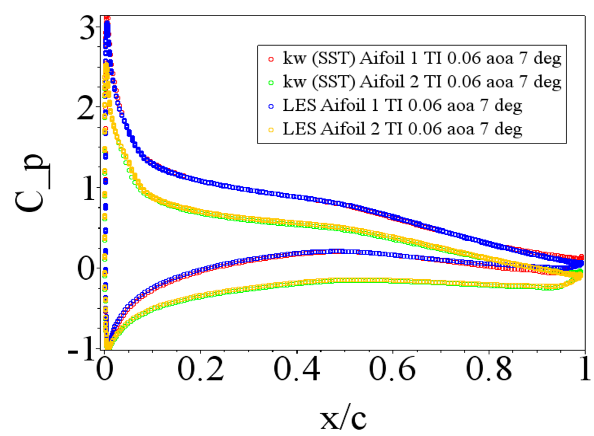

(d)

Figure 16: Cp vs x/ch for kw(SST) and LES model, (a) AoA of 0 deg with TI of 1%, (b) AoA of 0 deg with TI of 6%, (c) AoA of 7 deg with TI of 1% and (d) AoA of 7 deg with TI of 6%

In Figure 16, curves of LES are added for *AoA* of *0 deg* and *7 deg* with turbulent intensity of *1%* and *6%*. These curves are compared with k omega (SST) model since the three RANS models give similar results. For the case of *AoA* of *0 deg* (Figure 16a), the difference in area under the curve is smaller compared with the k omega (SST) model since it can capture the variations of pressure produced by the instantaneous velocities. It is important to pay special attention to the difference in area under the curve, since this net area is proportional to the net aerodynamic force over the airfoil. In the case of airfoil 1, it has a smaller area difference under the curve, with respect to airfoil 2; because of the throat effect formed by the adjacent airfoil that produces higher velocities in the pressure side decreasing the amount of pressure. Comparing the LES curves of Figure 16a and Figure 16b, the difference of area under the curve of Figure 16b is greater that in Figure 16a, this is produced by the difference in turbulence intensity. Since in Figure 16b the turbulence intensity is higher, the magnitudes of the pressure coefficient in the suction side increases, meaning that the amount of pressure decreases and the velocity increases for this region.

For the *AoA* of *7 deg*, the curves of Figure 16c and Figure 16d have a similar behavior and magnitude. The increment in turbulent intensity, did not seem to affect the curve of pressure coefficient.

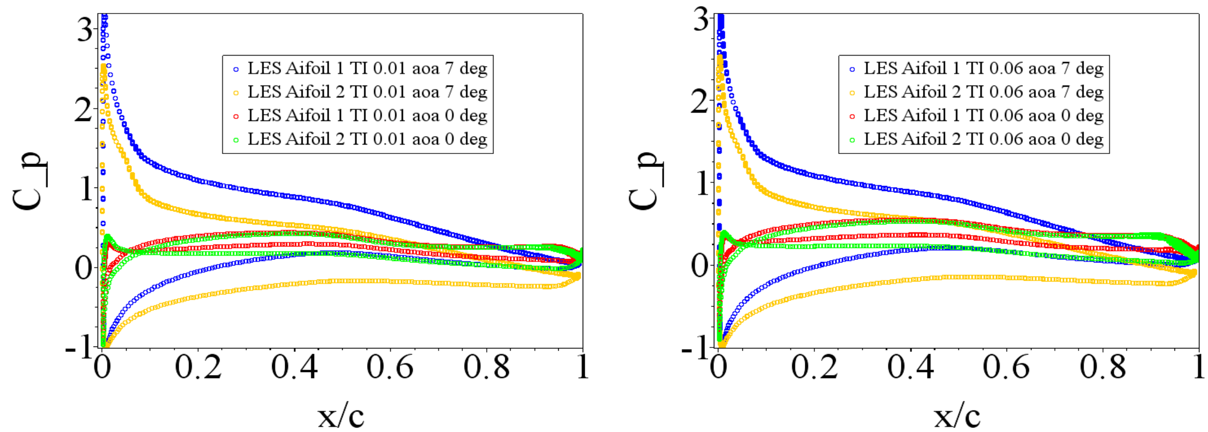

(a) *(b)*

Figure 17: Cp vs x/ch for LES model, (a) AoA of 0 deg and 7 deg with TI of 1%, (b) AoA of 0 deg and 7 deg with TI of 6%

Figure 17 shows a comparison between the pressure coefficient of the LES model for *AoA* of *0 deg* and *7 deg*, it can be observed that the difference in area under the curve is significant in both plots (Figure 17a and Figure 17b). The curve for *AoA* of *7 deg* encloses a bigger area since the velocity near the surface of the airfoils increase because the flow is accelerating, this provokes the pressure to decrease and coefficient of pressure to increase. In the case of turbulent intensity, the same observations can be done as in the previous plots, where at *AoA* of *0 deg* there is a difference in the magnitudes of the pressure coefficient between Figure 17a and Figure 17b, because of the increment in turbulence intensity. Meanwhile, at *AoA* of *7 deg*, this difference cannot be perceived.

4.2 Boundary Layers

As shown is Figure 18, boundary layer curves are obtained at pressure tap 1 located at *16%* of the chord in airfoil 2.

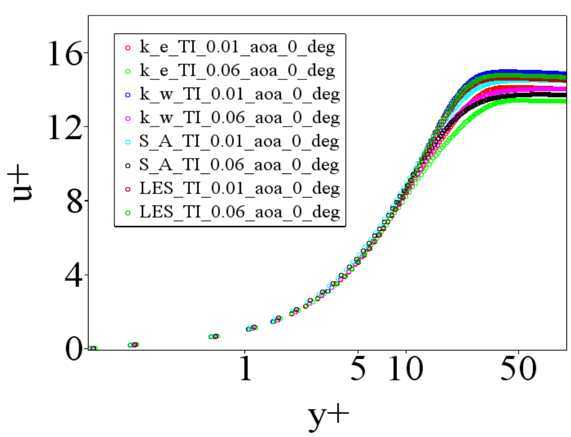

(a)

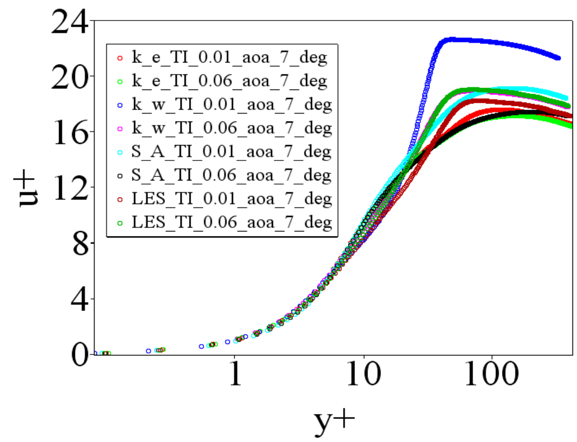

(b)

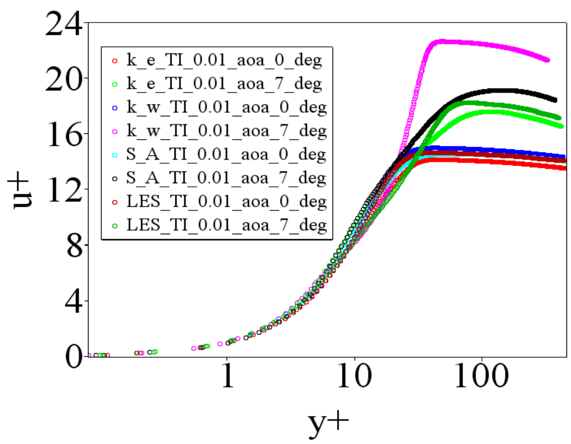

(c)

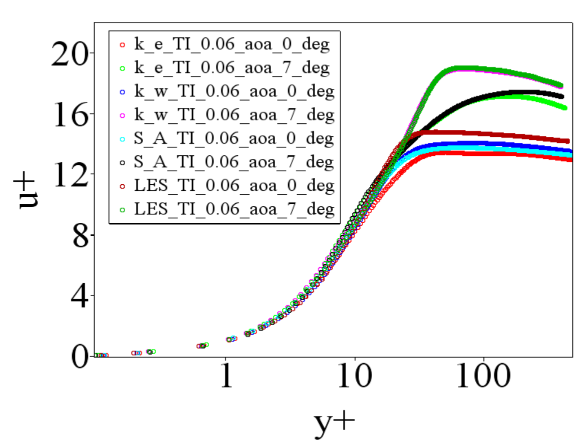

(d)

Figure 18: u+ vs y+ Pressure Tap 1 airfoil 2, (a) RANS models and LES for TI of 1% and 6% with AoA of 0 deg, (b) RANS models and LES for TI of 1% and 6% with AoA of 7 deg, (c) RANS models and LES for AoA of 0 deg and 7 deg with TI of 1% and 6%, (d) RANS models and LES for AoA of 0 deg and 7 deg with TI of 1% and 6%

In Figure 18a, boundary layers of the airfoil 2 at pressure tap 1 are plotted for turbulence intensities of *1%* and *6%*; for an *AoA* of *0 deg*. Overall, the RANS and LES models give similar results for $0 < y+ \leq 30$. The major difference is due to the increment in turbulence intensities, except for the LES model. For instance, when the turbulence intensity increases, the magnitude of u+ decreases in the outer region of the boundary layer, this phenomenon can be seen in the three

RANS models, but in the LES model; the curve of the boundary layer with turbulence intensity of *1%*, seems to collapse with the curve of *6%*.

For the case of Figure 18b, the same behavior is noted for the change in turbulence intensity as in Figure 18a for the RANS models. The magnitudes of *u+* are greater since the *AoA* is increased to *7 deg*, meaning that the flow velocity is increasing because of the increment in the *AoA*. Comparing the behavior of the boundary layers of the RANS models, it can be seen that the realizable two layers k epsilon and Spalart Allmaras model are similar in behavior. In the case of k omega (SST), higher values of *u+* are observed with respect to the other RANS models; specially for *AoA* of *7 deg*. Since k omega (SST) is an hybrid of standard k omega and standard k epsilon, it is more sensible to external effects as pressure gradients or turbulence intensities. For this scenario, the LES behaves different than the RANS models, because the magnitude of *u+* in the boundary layer for a higher turbulence intensity increases instead of decreasing. Therefore, the LES model captures a behavior that is not common since in most of the cases. Prediction that this behavior might be due to the fact that the flow is highly three-dimensional and it will be looked at in more detail in section 4.3, 4.4 and 4.5. The values of *u+* decreases at higher values of turbulence intensities (Torres-Nieves, 2011). Moreover, the magnitudes of *u+* for the LES vs the RANS models, it can be noted that, for a turbulence intensity of *6%,* the curve of LES and k omega (SST) collapse. For the case of *1%* of turbulence intensity, LES and k omega models also predict boundary layers with similar *u+* magnitudes.

In Figure 18c, for a turbulence intensity of *1%*, curves of the boundary layer for the RANS and LES models are plotted for *AoA* at *0 deg* and *7deg*; hence, isolating the effect of *AoA*. When comparing the curves for *AoA* of *0 deg*, the magnitudes of *u+* are similar, in contrast with *AoA* of *7 deg* were the differences in magnitude of *u+* are significant. Spalart Allmaras, realizable two layers k epsilon and LES model have different values of *u+*, but they are in the same range. In the other hand, the values of *u+* for the k omega (SST) in the outer region of the boundary layer overshoots in comparison with the other models.

Figure 18d shows a similar behavior to Figure 18c, the difference is the turbulence intensity magnitude; that is *6%*; is producing smaller values in magnitude of *u+*. It can be observed that the values of *u+* for the k omega (SST) curve are in the same range than the other RANS and LES models. Moreover, it has similar values of *u+* with respect to the LES model curve; also seen in Figure 18b.

Now, the boundary layers are obtained for pressure tap 5; that is at *74%* of the chord in airfoil 2 as shown in Figure 13. In Figure 19a boundary layer curves are plotted for turbulent intensities of *1%* and *6%* for an *AoA* of *0 deg*. Compared with pressure tap 1, the values of *u+* are higher in magnitude due to acceleration in the flow produced by the curvature of the airfoil. The RANS models have *u+* values that are in the same range. In the case of k omega (SST), like in the other cases, has higher values of *u+* than the rest. For the case of the LES simulations, it can be observed that for small values of *y+*, *u+* has negative values. Therefore, this means that the velocity of the flow in this region is going opposite to the chordwise flow direction.

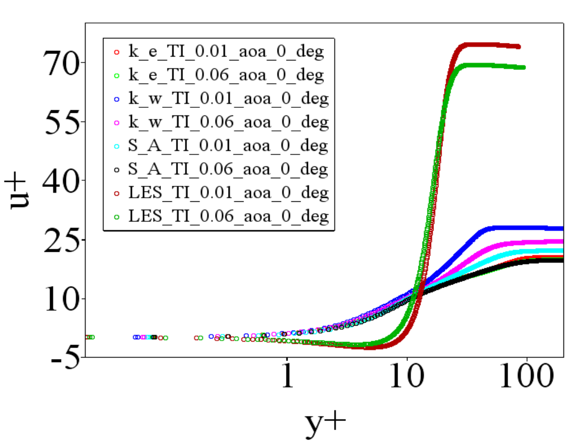

(a)

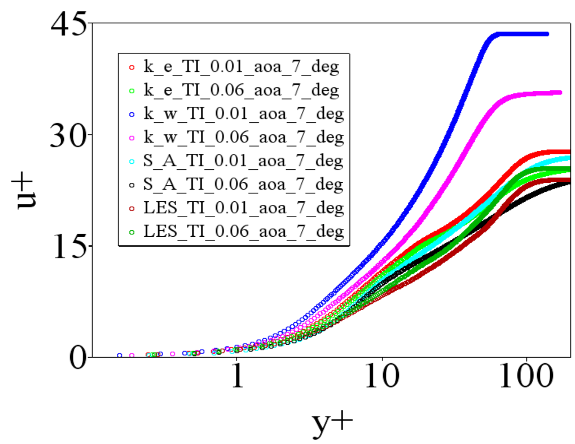

(b)

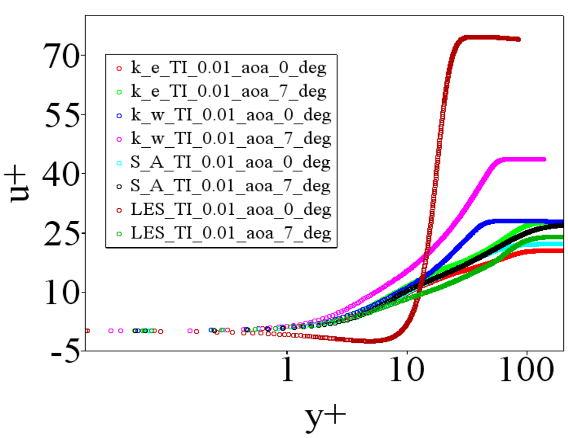

(c)

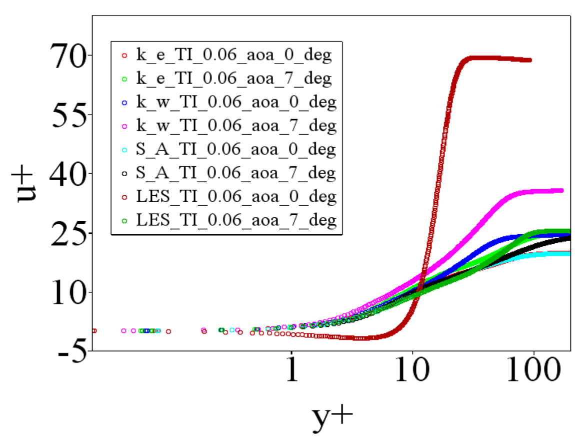

(d)

Figure 19: u+ vs y+ Pressure Tap 5 airfoil 2, (a) RANS models and LES for TI of 1% and 6% with AoA of 0 deg, (b) RANS models and LES for TI of 1% and 6% with AoA of 7 deg, (c) RANS models and LES for AoA of 0 deg and 7 deg with TI of 1% and 6%, (d) RANS models and LES for AoA of 0 deg and 7 deg with TI of 1% and 6%

Since the data of $u+$ is obtained with the mean velocity, separation of fluid in this point cannot be predicted only by analyzing this plot because statistically the values of the instantaneous velocity, in the opposite direction of the mean velocity, can prevail; but physically the flow separation can be instantaneous. This means that there are instants were the flow is separated, and in other instances the flow is attached. This is studied in more detail in section 4.3. Also, in the LES model; it can be observed that the values of $u+$, for the high values of $y+$, are greater than those RANS predicted by. In the case of the increment in turbulence intensity, the LES model and the rest of the RANS models are predicting that the values of $u+$ decreases.

For the case of Figure 19b, were the *AoA* is increased to *7 deg*, the behavior of the LES is completely different. Now the magnitudes of $u+$ are in the same range than the realizable two layers k epsilon and the Spalart Allmaras model. Also, for a higher turbulence intensity the value of $u+$ increases instead of decreasing. In the case of the RANS models, k omega (SST) has an overshoot for the values of $u+$ in comparison to the rest of the models. For the increment in turbulence intensity, all the RANS models behave the same; since the values of $u+$ decreases. In Figure 19c the difference in magnitudes of $u+$, compared for *AoA* of *0 deg* and *7 deg* is more notable than in Figure 19d. This means that for the turbulence intensity of *1%*, the difference between boundary layers velocity magnitude $u+$ is bigger than the difference between the boundary layers velocity magnitude $u+$ at a turbulence intensity of *6%*.

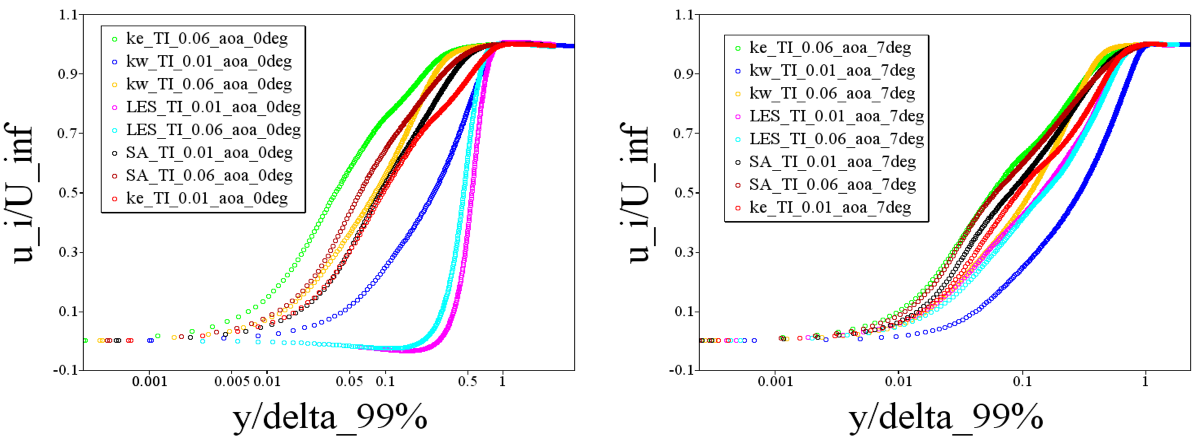

(a) *(b)*

Figure 20: u_i/U_inf vs y/delta_99% Pressure Tap 5 airfoil 2, (a) RANS models and LES for TI of 1% and 6% with AoA of 0 deg, (b) RANS models and LES for TI of 1% and 6% with AoA of 7 deg

Figure 20 presents the mean velocity profiles in outer scaling at *74%* chord, for different turbulent intensities and angles of attack. The edge of the boundary layer was considered at *99%* of the local free stream velocity. It is observed that the boundary layer curves are more sensitive to the change in turbulent intensities using this scaling. Also, in Figure 19 there is a significant difference in magnitude between the *u+* values of the LES curves vs the RANS curves; at *0 deg*. This behavior is expected since the values of the shear velocity in regions of flow separation are low. Meanwhile, in Figure 20, for an angle of attack of *0 deg* the LES and RANS models have similar magnitudes of *u_i/U_inf*; however, LES model is capturing recirculation flow.

4.3 Flow Separation

To investigate flow behavior in airfoil 2 at the location of pressure tap 5 for an *AoA* of *0 deg*, in addition to the boundary layer curves in Figure 19a, c, d, 20a and b, skin friction coefficient and instantaneous velocity contours at different times are presented.

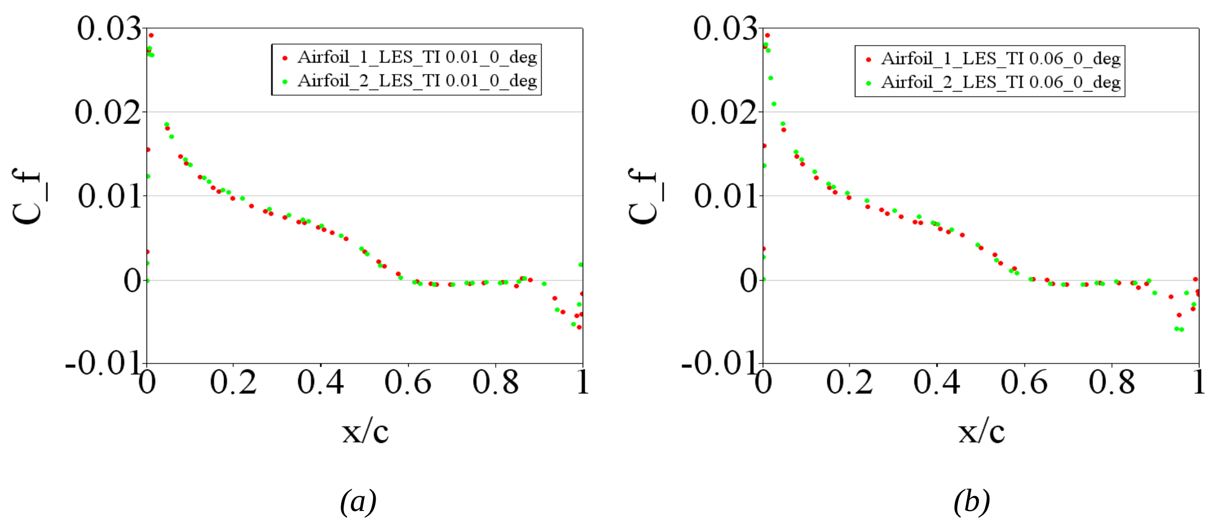

Figure 21: C_f vs x/c Pressure Tap 5 airfoil 1 and 2 LES Model, (a) TI of 1% with AoA of 0 deg, (b) TI of 6% with AoA of 0 deg

Figure 21 presents the values of the skin friction coefficient for airfoil 1 and 2, at different turbulent intensities with an angle of attack of *0 deg*. Comparing airfoil 1 and 2, skin friction coefficients are similar in magnitude and behavior; the same phenomenon is observed by increasing the turbulent intensity. Figure 21a demonstrates flow recirculation (i. e, negative values) at approximately *63%* chord for 1% turbulent intensity. For a turbulence intensity of 6% this occurs at approximately *68%*.

In order to estimate the location where the flow transitions from laminar to turbulent, the skin friction coefficient correlation for a flat plate developed by Smits *et al.* (1983) was used. Since the correlation was developed for a flat plate, it can be used only as an approximation to estimate the location of the transition point. In order the calculate the skin friction coefficient using Smits *et al.* (1983) correlation, the Reynolds number based on the momentum thickness (Re_θ) was assumed to be the lowest in order to maintain turbulent flow on a flat plate; that is, $Re_\theta = 300$. The value of the friction coefficient at the location of transition was *0.005767*. With this value, the approximate location of the transition point was obtained from Figure 21a and b: *41.8%* chord and *43.7%* chord, respectively. These are in agreement with results of experimental data provided by Schreiber *et al.* (2002), where for low Reynolds numbers, the location of the transition point is 35% - 40% chord.

In the instantaneous velocity contours, if negative velocities persist near the wall region at the location of pressure tap 5, then it can be concluded that there is flow separation in this region. Instantaneous velocities contours where created for four dimensionless time (*t+*) of *t+=0*, *t+=10*, *t+=100* and *t+=500*. The scale time is defined as the Kolmogorov scale time when *t+≈1*. This dimensionless time was selected in order to compare the contours by a turbulent time scale.

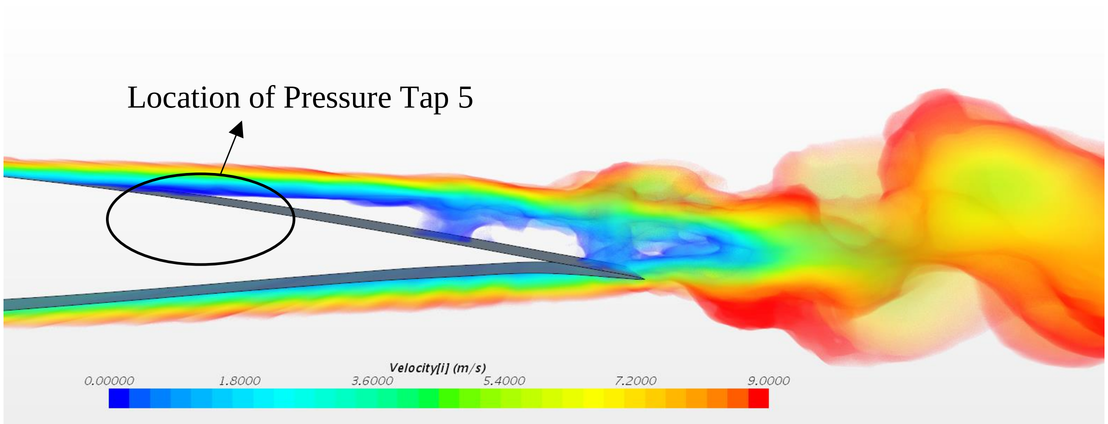

Figure 22: Instantaneous Velocity Contour t+=0

In the case of *t+=0*, it refers to the first contour captured when the simulation converged statistically, the *t+=10* means that the second contour was captured after ten times the time scale; for contour 3 and 4 the same analogy is done for a *t+=100* and *t+=500*. The blank space near the wall region show negative velocities; no color was assigned to make the separation region easier to visualize. In Figures 22, 23, 24 and 25, it can be observed that the flow separation in the location of pressure tap 5 persists. Therefore, separation of flow occurs in the location of pressure tap 5 on airfoil 2 for *AoA* of *0 deg*. This demonstrates the ability of LES to capture three-dimensional effects on the flow. Since it is a transient and three-dimensional model, it can capture the flow behavior at different times and space coordinates.

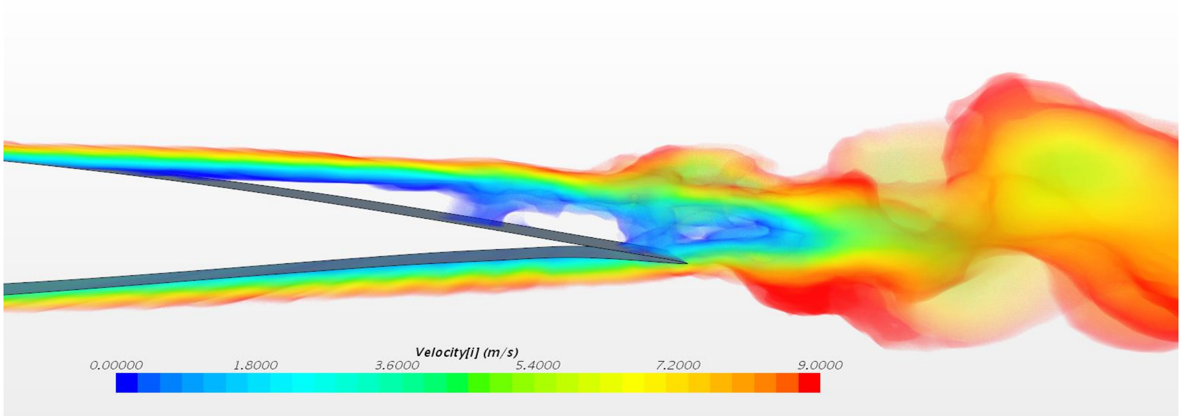

Figure 23: Instantaneous Velocity Contour t+=10

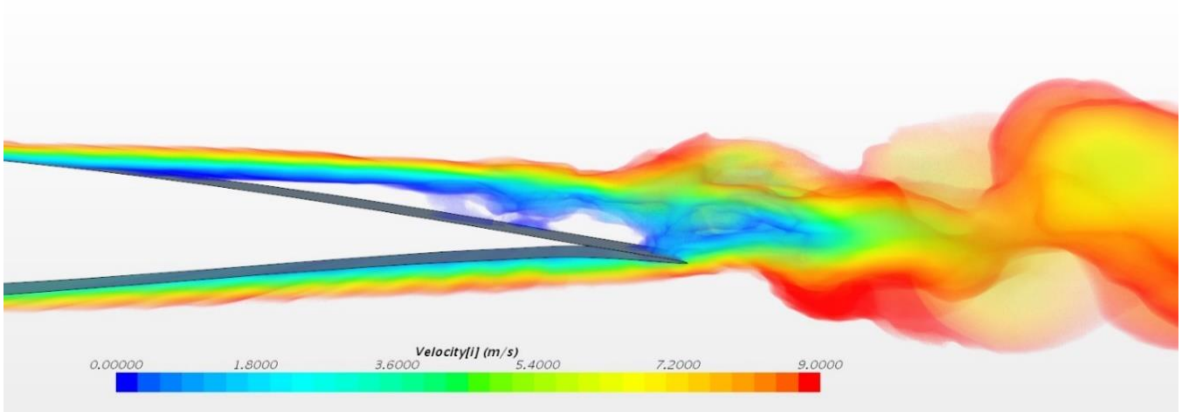

Figure 24: Instantaneous Velocity Contour t+=100

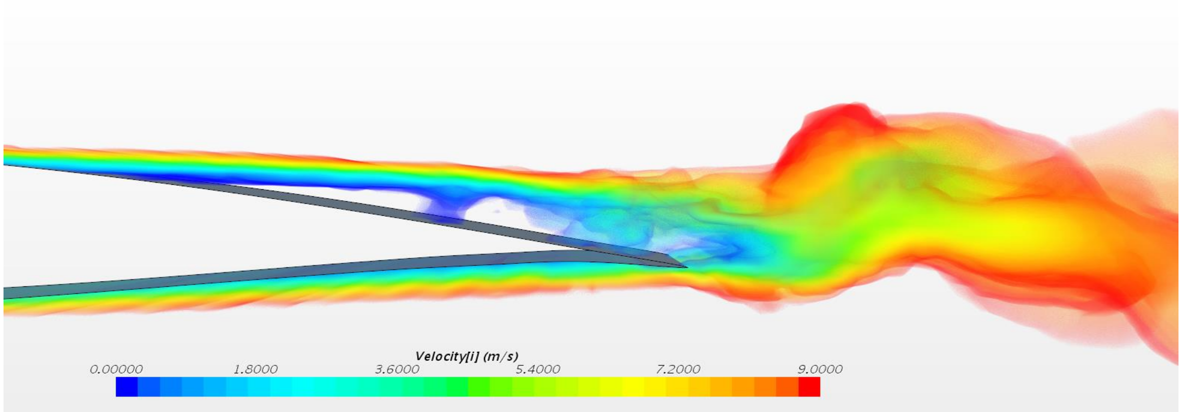

Figure 25: Instantaneous Velocity Contour t+=500

4.4 Turbulence Intensity Effects

Figure 26 compares the effect of turbulence intensity, at different angles of attack, for the two airfoils as predicted by the LES model.

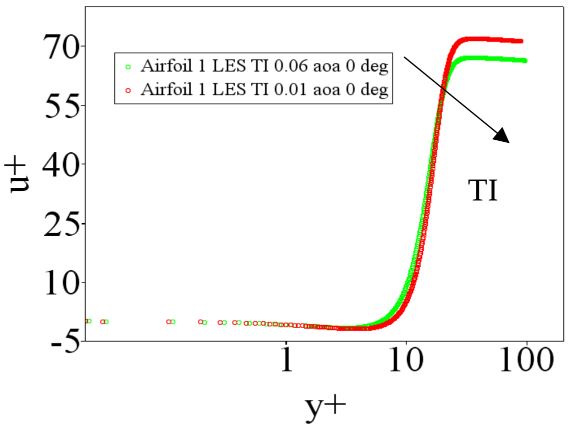

(a)

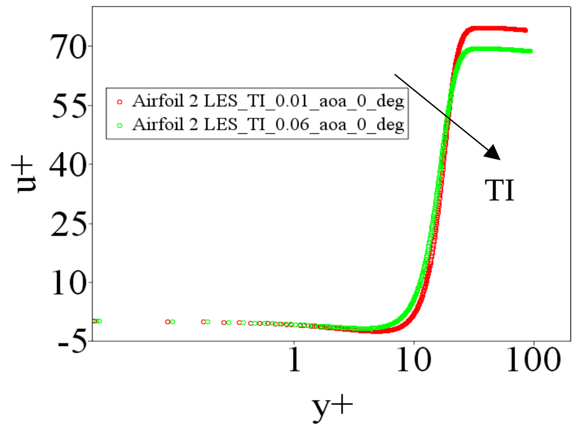

(b)

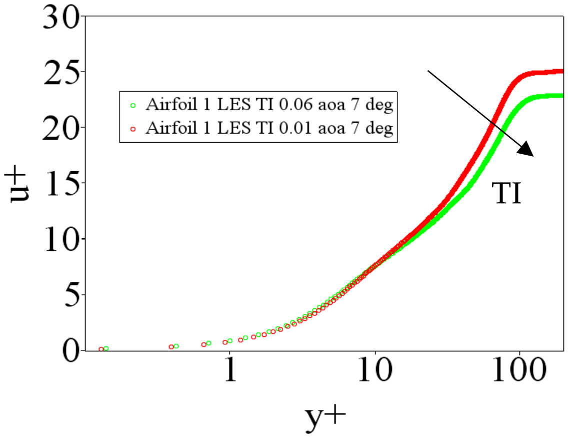

(c)

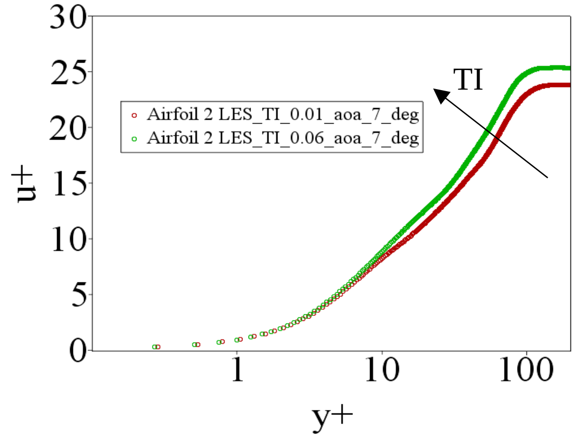

(d)

Figure 26: u+ vs y+ LES Pressure Tap 5, (a) Airfoil 1 for TI of 1% and 6% with AoA of 0 deg, (b) Airfoil 2 for TI of 1% and 6% with AoA of 0 deg, (c) Airfoil 1 for TI of 1% and 6% with AoA of 7 deg, (d) Airfoil 2 for TI of 1% and 6% with AoA of 7 deg

It can be observed in more detail the difference in the magnitudes of $u+$ for the LES model, where the boundary layer of pressure tap 5 in airfoil 1 (top airfoil) is compared with pressure tap 5 of airfoil 2. For Figure 26a and Figure 26b it is evident that when the turbulence intensity increases the values of $u+$ decreases. Figure 26c, the LES model for airfoil 1, also follows the same behavior. On the other hand, in Figure 26d, *AoA* at *7 deg*, the LES model has a different prediction for airfoil 2 at *AoA* of *7 deg*; since the value of *u+* increases when the turbulence intensity increases. This is a peculiar scenario since in most cases in turbulent flow experimentation, this behavior is not seen. Rather turbulent intensity tends to decrease the values of u+ (Torres-Nieves, 2011). As pointed out by Torres-Nieves (Thesis, 2011), this phenomenon occurs when multiple external conditions are present and the flow becomes highly three-dimensional. LES is able to capture this behavior since it can obtain instantaneous velocities more detailed at time differences near to the Kolmogorov scale. Therefore, behaviors of the boundary layer can be obtained since the values of the average velocities and their fluctuations are more accurate. The effect of the increment in *u+* due the increment in turbulence intensity only occurs in airfoil 2 at *AoA* of *7 deg*, more than likely due to the strong pressure gradient that is experienced by this airfoil.

4.5 Velocities Fluctuations

In trying to understand the complexity of the flow, velocity fluctuations were studied in three directions. In Figure 27a, the velocity fluctuation in the stream wise direction (*u'+*), for turbulence intensities of *1%* and *6%* at *AoA* of *0 deg* for airfoil 1 and 2, can be observed.

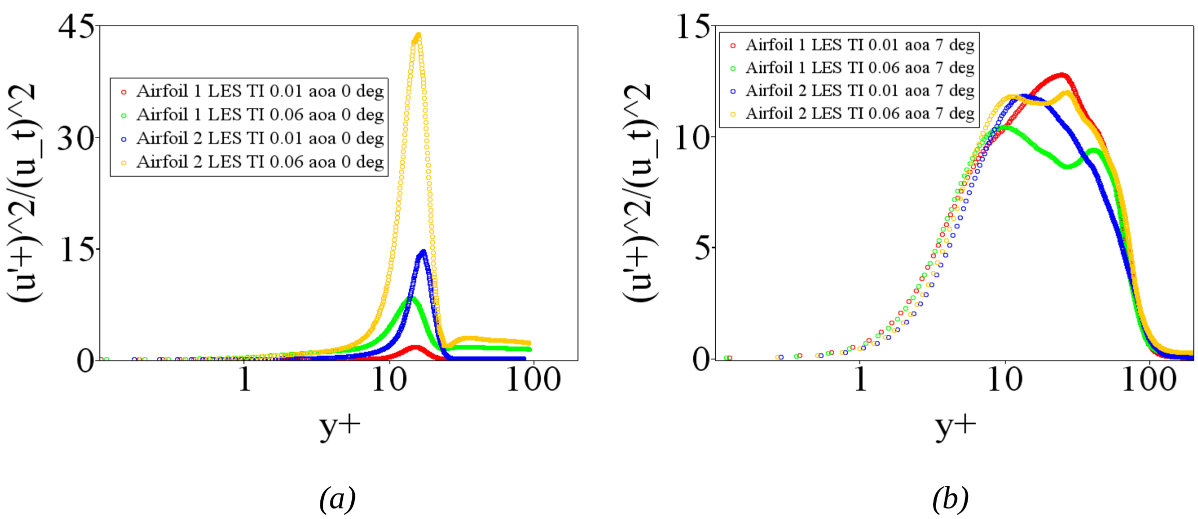

Figure 27: LES Model (a) u'+ vs y+ TI 1% and 6% at AoA of 0 deg, (b) u'+ vs y+ TI 1% and 6% at AoA of 7 deg

Comparing the curves at different turbulence intensities, the magnitude of *u'+* are greater for the turbulence intensity of *6%* than from the one of *1%*. Now, for the case of airfoil 1 and 2, the magnitudes of *u'+* are higher for airfoil 2 in both cases; for a turbulence intensity of *1%* and *6%*. For airfoil 2 at a turbulence intensity of *6%*, the value of *u'+* exceed dramatically the other curves values. This phenomenon occurs since it appears that there is flow separation, and with a high value of turbulence intensity, the instantaneous velocities in the stream wise direction have significative changes in magnitude.

In Figure 27b, the *AoA* is increased to *7 deg*. The magnitudes of *u'+* are similar. However, the area under the curve for the four curves are greater than in Figure 27a. Also, contrary to Figure 27a, the magnitude of *u'+* for airfoil 1 increases when the turbulence intensity decreases. On the other side, in airfoil 2 the magnitude of *u'+* stays almost the same for the two cases of turbulence intensity of *1%* and *6%*.

In Figure 28a, the velocity fluctuation in the normal direction of the wall (*v'+*) is plotted for airfoil 1 and 2 with turbulence intensities of *1%* and *6%* at *AoA* of *0 deg*. The behaviors of the curves are similar to Figure 27a, except for the magnitudes of *v'+*; these are smaller with respect to *u'+*. It can be observed that in the outer region, the shape of curves of *v'+* with a turbulence intensity of *6%* differ in comparison with the curves that have a turbulence intensity of *1%*. In Figure 28b the curves are plotted for an *AoA* of *7 deg*. Comparing with Figure 28a, it can be observed that the values of *v'+* for the four curves are significantly higher in magnitude; also, the area under the curve is greater. Like in Figure 27b, for airfoil 1 the values of *v'+* increases as the turbulence intensity decreases. Meanwhile, in airfoil 2 the values of *v'+* increases as the turbulence intensity increases. Also, it can be observed that the curve of airfoil 1 and 2 for a turbulence intensity of *6%* are approximately the same in behavior and magnitude; provoking that one curve overlaps with the other.

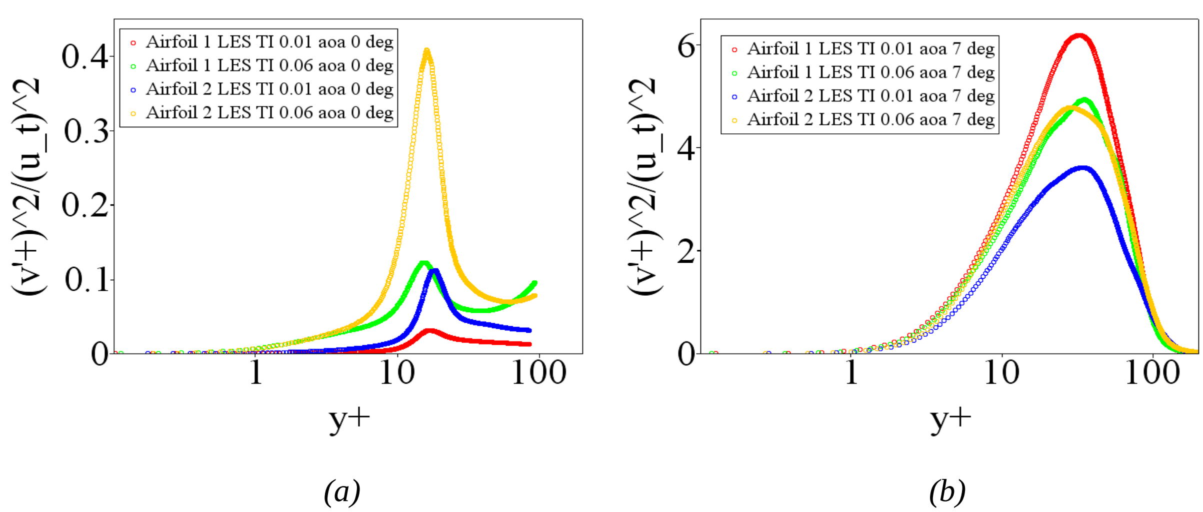

Figure 28: LES Model (a) v'+ vs y+ TI 1% and 6% 0 deg, (b) v'+ vs y+ TI 1% and 6% 7 deg

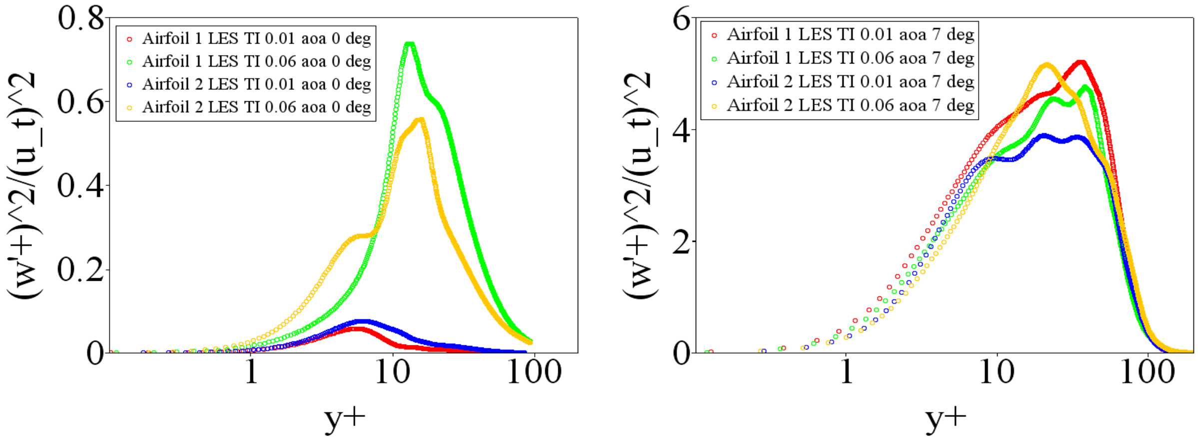

(a) *(b)*

Figure 29: LES Model (a) w'+ vs y+ TI 1% and 6% 0 deg, (b) w'+ vs y+ TI 1% and 6% 7 deg

In Figure 29a, curves of velocities fluctuations in the spanwise (*w'*+) are plotted for turbulence intensities of *1%* and *6%* with an *AoA* of *0 deg*. For this case, the values of *w'*+ for airfoil 1 and 2 are greater for a turbulence intensity of *6%*. In the case of a turbulence intensity of *1%*, the values of *w'*+ are almost insignificant in comparison with the values of turbulence intensity of *6%*. It can be observed that the values of *w'*+ for airfoil 1 and 2 with a turbulence intensity of *1%* are approximately equal, the same phenomenon occurs with a turbulence intensity of *6%*. For Figure 29b, an *AoA* of *7 deg* is applied. The values of *w'*+ are considerably higher than in Figure 29a, also it can be seen that the curves have similar behaviors between them and that the magnitude of *w'*+ is in the same range. The area under the curve is greater in Figure 29b than Figure 29a, however the difference is not so pronounced like in the velocities fluctuations *u'*+ and *v'*+ curves. For the case of airfoil 1, when the turbulence intensity increases, the magnitudes of *w'*+ decreases. In the other hand, in airfoil 2 the magnitudes of *w'*+ increases when the turbulence intensity increases.

4.6 Boundary Layer Thickness

For the case of the *y*+ value at the edge of the boundary layer (Δ*y*+), the minimum value was Δ*y+=26* located *16%* chord for the k-omega model with a turbulent intensity of *1%* and an angle of attack at *0 deg*. The maximum value was Δ*y+=370* for the model of k-epsilon located at *74%* chord with a turbulent intensity of *6%* and an angle of attack at *7 deg*.

CHAPTER 5: CONCLUSION

The first objective, of this study was to perform a simulation with an overset mesh, using different RANS models to understand the behavior of boundary layers. It was successfully achieved. An overset mesh was created with a polyhedral mesh, obtaining the desired communication between the overset and background, thanks to a smooth transition produced by an overlap volumetric control. For the case of the aerodynamic performance, the three RANS models employed (Spalart Allmaras, realizable two layers k epsilon and k omega (SST)) predicted similar curves for the pressure coefficient with turbulence intensities of *1%* and *6%* at *AoA* of *0 deg* and *7 deg*. For an *AoA* of *7 deg*, the difference in the area under the curve is greater than for an *AoA* of *0 deg*, since the flow has a higher acceleration, producing higher increment in velocity and decrement in pressure. Significant differences are observed among the pressure coefficients for airfoil 1 and 2. This phenomenon is produced because both bodies form a throat that accelerates the fluid producing changes in the pressure field observed at the pressure side of airfoil 1 and the suction side of airfoil 2. For the analysis of the boundary layers, the three RANS models gave similar results for the position at *16%* chord for an *AoA* at *0 deg* and a turbulence intensity of *1%*; external conditions do not seem to be influencing their development. For the case of a turbulence intensity of *6%*, a slight difference is appreciated because the free stream flow has more velocity fluctuations due to the increment in turbulence intensity. For the case of an *AoA* of *7 deg*, the magnitudes of $u+$ are higher and the difference between the k omega (SST) model and the other models is notable; this suggests that it overpredicts the values of $u+$ with respect to the other RANS models. In the position at *74%* chord (closer to the trailing edge) differences are seen in the modeling of the boundary layer, especially for the case of k omega (SST) that has higher values of $u+$ than the rest of the models for turbulence intensities of *1%* and *6%* at *AoA* of *0 deg* and *7 deg*. This indicates that k omega also overestimated the values of $u+$ in the position at *74%* chord.

Objective two was executed since the pressure coefficients and boundary layers were compared with a Large Eddy Simulation (LES). For the case of *AoA* at *0 deg*, with turbulence intensities of *1%* and *6%*, the LES curve of the pressure coefficient behaves different than the ones of RANS models. The difference in area under the curve is smaller and the deflection in the suction side of both airfoils is more pronounced. These differences can be produced because the LES model was able to capture flow separation, meanwhile RANS models were not able to capture it. For the case of an *AoA* of *7 deg* with turbulence intensities of *1%* and *6%*, the curves of the pressure coefficient were similar between the LES model and the three RANS models. In trying to understand this effect, it was found that the velocity fluctuations in the three directions, at *AoA* of *7 deg* captured by LES are in the same order of magnitude; this is in agreement when compared to the assumption of the RANS models, that the velocities fluctuations are isotropic. Therefore, the values of the pressure field are similar in both models. For the case of the boundary layers, at an *AoA* of *0 deg* for turbulence intensities of *1%* and *6%*, at *16%* chord, the values of LES model are similar to the RANS values. On the other hand, at *74%* of the chord, the LES model captured a flow separation that RANS models were not able to capture. Therefore, RANS models cannot predict flow separation as early as the LES model does. With the correlation of skin friction coefficient developed by Smits *et al.* (1983) for a flat plate, approximate values for the location of the transition point were obtained. For *AoA* of *0 deg* and *TI* of *1%*, the transition occurs at approximately *41.8%* chord, whereas for *TI* of *6%*, it is observed at *43.7%* chord. In the case of an *AoA* of *7 deg* with turbulence intensities of *1%* and *6%*, the boundary layer curves of the LES model and RANS models were similar. Since the velocities fluctuations of LES model at an *AoA* of *7 deg* are similar in magnitude, this can be comparable with the RANS models' main assumption of isotropic velocities fluctuations. For the case of the LES model for an *AoA* of *7 deg*, in airfoil 2 at *74%* chord, the values of *u+* for a turbulence intensity of *6%* are higher than for a turbulence intensity of *1%*. Therefore, in airfoil 2 the values of *u+* increase as the turbulence intensity also increases. This phenomenon can be due to the changes in the velocity fluctuations observed in airfoil 1 and 2.

Finally, the third objective was fulfilled. Numerical simulations were validated with experimental data of pressure coefficients for airfoils 1 and 2. The experiments used for these comparisons were performed by graduate student Wilmer A. Martinez Valle. Although there are some differences between the experimental data and LES, both curves follow a similar behavior.

CHAPTER 6: FUTURE WORK

The research work presented here demonstrated important aspects of the behavior of boundary layers for adjacent blades. There are some questions that deserve to be studied in more detail. For instance; wall resolution of the LES model, the values were: normal to the wall distance $y^+ < 1$, chord distance $x^+ = 130 \cdot y^+$ and the spanwise direction $z^+ = 40 \cdot y^+$. For future investigations, modifications of the chord and spanwise distance can be done to obtain lower values to increment the near wall resolution. (Sarlak *et al.*, 2014) recommended values of $50 \leq x^+ \leq 130 \cdot y^+$ and $15 \leq z^+ \leq 130 \cdot y^+$. Also, for the LES model a dimensionless time (t^+) was set to be $t^+ = 10$. This value can be reduced to be closer to the Kolmogorov time scale ($t^+ \approx 1$). The amount of time to capture the statistical data for average velocities and their fluctuations, was five times the reference time value. This amount of time can be extended to obtain a major amount of data for statistical analysis.

Other important study that can be done in the future is to analyze the two airfoils compressor cascade NACA 65-410 at different angles of attack higher than *0 deg* but lower than *7 deg*. To have a better knowledge of the behavior of boundary layers at the suction side of airfoil 1 and 2, experimental data of the velocities and it fluctuations need to be obtained in order to compare with numerical data. Instead of modeling a NACA 65-410 compressor cascade of two airfoils, a NACA 65-410 of three airfoils compressor cascade can be simulated to analyze the performance of the airfoil with the changes in the pressure field of the suction and pressure side.

References

Abe, K., Kondoh, T. and Nagano Y. (1994). "A new turbulence model for predicting fluid flow and heat transfer in separating and reattaching flows-I. Flow field calculations", Int. J. Heat Mass Transfer. Vol(37), pp. 139-151.

Aksnes, N. Y. (2015) *Performance Characteristics of the NREL s826 Airfoil* (Master's Thesis, NTNU Trondheim, Norway).

Aungier, R. H. (2003). *Axial-Flow Compressors a Strategy for Aerodynamic Design and Analysis* (The American Society of Mechanical Engineers Three Park Avenue, N.Y.). Chap. 6, pp. 117-120.

Balzer, W. and Fasel, H. F. (2010). "Direct Numerical Simulation of Laminar Boundary-Layer Separation and Separation Control on the Suction Side of an Airfoil at Low Reynolds Number Conditions", AIAA. pp. 1-20.

Camp, T. R. and Shin, H. W. (1994). "Turbulence Intensity and Length Scale Measurements in Multistage Compressors", ASME Journal. pp. 1-10.

CD-adapco, (2014). *STAR-CCM+ Version 9.04 User Guide*. pp. 3393-3495.

Clemens, N. T. and Narayanaswamy, V. (2014). "Low-Frequency Unsteadiness of Shock Wave/Turbulent Boundary Layer Interactions", Annual Review of Fluid Mechanics. pp. 469-492.

Dash, A. (2016). "CFD Analysis of Wind Turbine Airfoil at Various Angles of Attack", IOSR Journal of Mechanical and Civil Engineering. Vol(13), pp. 18-24.

Floros, M. W. and Sitaraman, J. (2010). "Parallel Unsteady Overset Mesh Methodology for Adaptive and Moving Grids with Multiple Solvers", NATO/RTO. pp. 1-24.

Gad-el-Hak, M. (2016). "Nine Decades of Fluid Mechanics", Journal of Fluids Engineering. Vol(138), pp. 1-10.

George, W.K. and Castillo, L. (1997) "Zero-pressure gradient turbulent boundary layer", Applied Mechanics Reviews. Vol(50), pp. 689-729

Gourdain, N., Sicot, F., Duchaine, F. and Gicquel, L. (2014). "Large eddy simulation of flows in industrial compressors: a path from 2015 to 2035", The Royal Society. pp. 1, 2.

Hoke, C. M., Decker, R. K., Cummings, R. M., McDaniel, D. R. and Morton, S. A. (2009). "Comparison of Overset Grid and Grid Deformation Techniques Applied to 2-Dimensional NACA Airfoils", AIAA, pp. 1-11.

Horlock, J. H. and Lakshminarayana, B. (1973). “Secondary Flows: Theory, Experiment, and Application in Turbomachinery Aerodynamics”, Annual Review of Fluid Mechanics. pp. 247-280.

Khazaei, H., Madadi, A. and Kermani, M. J. (2011). “Assement of Various Inviscid-Wall Boundary Conditions: Applications to NACA 65 Compressor Blade”, ASME. pp. 1-8.

Laborderie, J., Duchaine, F., Vermorei, O. and Gicquel, L. (2016). “Application of an Overset Grid Mehtod to the Large Eddy Simulation of a High-Speed Multistage Axial Compressor”, ASME. pp. 1-13.

Launder, B. E. (1988). “On the Computation of Convective Heat Transfer in Complex Turbulent Flows”, ASME. Vol(110), pp. 1112-1128.

Madadi, A., Kermani, M. J. and Khazaei, H. (2015) “Improvement of a solution of inviscid compressible flows using a mixed wall boundary condition”, Engineering Applications of Computational Fluid Mechanics. Vol(9), pp. 126-138.

Medic, G., Zhang, V., Wang, G., Joo, J. and Sharma, O. P. (2016). “Prediction of Transition and Losses in Compressor Cascades Using Large-Eddy Simulation”, Journal of Turbomachinery. Vol(138), pp. 1-9.

Menter, F. R. (1994). “Two-Equation Eddy-Viscosity Turbulence Models for Engineering Applications”, AIAA Journal. Vol(32), pp. 1598-1605.

Michálek, J., Monaldi, M. and Arts, T. (2012). “Aerodynamic Performance of a Very High Lift Low Pressure Turbine Airfoil (T106C) at Low Reynolds and High Mach Number With Effect of Free Stream Turbulence Intensity”, Journal of Turbomachinery. Vol(134), pp. 1-10.

Patankar, S. V. (1980). *Numerical Heat Transfer and Fluid Flow* (Hemisphere Publishing Corp., USA). Chap. 6, pp. 134.

Pope, S. B. (2000). *Turbulent Flows* (University of Cambridge, The Pitt Building, Trumpington Street, Cambridge, United Kingdom). Chap. 10, pp. 367, 370-375, 383 and 386. Chap. 13, pp. 560.

Post, S. (2011). *Applied and Computational Fluid Mechanics* (Jones and Bartlett Publishers, Sudbury, MA). Chap. 4, pp. 157, Glossary, pp. 507.

Sagmo, K. F., Bartl, J. and Saetran, L. (2016). “Numerical simulations of the NREL S826 airfoil”, Journal of Physics. pp. 1-10.

Sarlak, H., Mikkelsen, R., Sarmast S. and Sorensen, J. N. (2014). J. Phys.: Conf. Series 524

Schlighting, H. (1979). *Boundary-Layer Theory* (McGraw-Hill, Inc, USA). Chap. 1, pp. 3.

Schobeiri, M. T. and Abdelfattah, S. (2013). "On the Reliability of RANS and URANS Numerical Results for High-Pressure Turbine Simulations: A Benchmark Experimental and Numerical Study on Performance and Interstage Flow Behavior of Hight-Pressure Turbines at Design and Off-Design Conditions Using Two Different Turbine Designs", Journal of Turbomachinery. Vol(135), pp. 1-12.

Schreiber, H. A., Steinert, W. and Kusters, B. (2002). "Effects of Reynolds Number and Free-Stream Turbulence on Boundary Layer Transition in a Compressor Cascade", Journal of Turbomachinery. Vol(124), pp. 1-9.

Shan, H., Jiang, L. and Liu, C. (2005). "Direct numerical simulation of flow separation around a NACA 0012 airfoil", Computers and Fluids. pp. 1096-1114.

Shiyani, D. and Haria, A. (2012). "CFD Simulation of Flat Plate Aerodynamics at high angles of attack", pp. 1-5.

Singh, M. P., Khidiya, M. S. and Soni, S. (2016). "CFD Simulation of an Airfoil at different Angle of Attack", IJSRSET. Vol(2), pp. 773-776.

Smits, A. J., Matheson, N. and Jourbert, P. N. (1983). "Low-Reynolds-number turbulent boundary layers in zero and favorable pressure gradients", J. Ship Res. 27. Vol(3), pp.147-157.

Spalart, P. R. and Allmaras, S. R. (1994). "A one-equation turbulence model for aerodynamic flows", La Recherch Aérospatiale. pp. 5-21.

Spalart, P. R. and Rumsey C. L. (2017) "Effective Inflow Conditions for Turbulence Models in Aerodynamic Calculations", AIAA Journal. pp. 1-14.

Taylor, J. R. (1978). "Turbulence Measurement Addendum", NASA-Lewis Research Center. pp. 1-35.

Tennekes, H. and Lumley, J. L. (1972). *A First Course in Turbulence* (MIT Press, MA). Chap. 1, pp. 1-4.

Torres-Nieves, S. N. (2011). *Interaction Of Turbulent Length Scales With Wind Turbine Blades* (Rensselaer Polytechnic Institute Troy, NY). Chap. 7, pp. 129.

Walker, G. J. and Gostelow, J. P. (1989). "Effects of Adverse Pressure Gradients on the Nature and Length of Boundary Layer Transition", ASME Journal. pp. 1-11.

Wilcox, D. C., (1988). "Reassessment of the Scale-Determining Equation for Advanced Turbulence Models", AIAA Journal. Vol(26), pp. 1299-1310.

Zaki, T. A., Wissink, J. G., Rodi, W. and Durbin, P. A. (2010). "Direct numerical simulations of transition in a compressor cascade: the influence of free-stream turbulence", Journal of Fluid Mechanics. Vol(665), pp. 57-98.